2014

Variations in Salinity and Temperature on the Flank of an Offshore Louisiana Salt Structure

Candice M. McCollum
Louisiana State University and Agricultural and Mechanical College

VARIATIONS IN SALINITY AND TEMPERATURE ON THE FLANK OF AN OFFSHORE LOUISIANA SALT STRUCTURE

A Thesis

Submitted to the Graduate Faculty of the
Louisiana State University and
Agricultural and Mechanical College
in partial fulfillment of the
requirements for the degree of
Master of Science

in

The Department of Geology and Geophysics

by
Candice M. McCollum
B.S., University of Alaska, 2011
August 2014

Acknowledgements

Special thanks to my advisor, Dr. Nunn, and committee member, Dr. Hanor, for all of their support and expertise in this endeavor. Without Dr. Nunn's knowledge and relationship with the industry, this project never would have come to fruition. I am extremely grateful that Dr. Hanor was willing to offer constant support and guidance throughout this project. I also would like to thank Dr. Wicks for her willingness to step in and offer her input and advice on my committee.

Very special thanks to my friends and family who made this experience easier. I am very grateful for my husband, Lanse, for his love, patience, and support through the thick and thin of graduate school. Thank you Jie Shen, a good friend and classmate, for all the help and input throughout school and especially in Petrel.

I am especially grateful for the company that provided the data used in this project and for the many individuals who helped facilitate this data donation. Also, I'd like to thank John Kruger and BOEMRE for assisting me with acquiring the well header information used in this project.

Table of Contents

Abstract

Sediments located in the vicinity of salt structures in the northern Gulf of Mexico have highly complex structures and fluid dynamics associated with the dissolution and diapirism of salt. Past studies (Lin and Nunn, 1997; Bruno and Hanor, 2003; Richards, 2013) have shown that faults associated with salt structures can act both as migration pathways and barriers to the flow of formation waters. Bruno and Hanor (2003), Steen et al. (2011), and Richards (2013) also demonstrated that lithology was a controlling factor in the flow of formation waters. In this study, two sets of wireline logs, one used in salinity mapping and the other used in temperature mapping, combined with structural interpretations from a 3D seismic volume were used to investigate how faulting and lithology controlled the migration of saline formation waters above a near-shore salt structure in the northern Gulf of Mexico. By using the Revil et al. (1998) method of calculating salinity from continuous digital gamma and resistivity logs, along with other parameters, it was shown that sand-dominated intervals had higher salinity values than shaly intervals. The calculated salinity curves also demonstrate that salinity is much lower in the pore water of the shale-dominated overpressure zone (<100g/L) than in the overlying sand-dominated zone (100-250 g/L). Two areas were identified where faults offset salinity values, suggesting that faults may impede the flow of formation waters in this region and that some faults are younger than brine migration. Temperature and salinity mapping at two depths (6000 and 1000 ft SSTVD) combined with fault interpretations from seismic showed that faulted regions have elevated temperatures and salinities. This suggests that warmer formation waters are migrating upward along the fault from the deeper overpressured zone into the overlying hydrostatically pressured hypersaline zone, as suggested by Lin and Nunn (1997).

Introduction

In the Gulf of Mexico, elevated pore water salinity in sediments is mainly sourced by the dissolution of salt (Posey and Kyle, 1988; Hanor and Sassen, 1990). The original salinity of Gulf Coast sediments before burial was that of marine levels (35 g/L). After burial and interaction with dissolving salt structures, the sediments contain formation waters with extremely elevated salinity concentrations (up to 350 g/L). The distribution of these saline brines within Gulf Coast sediments is complex (Hanor and Sassen, 1990; Bruno and Hanor, 2003; Steen et al., 2011; Richards, 2013).

Three major hydrogeologic regimes have been identified in the vicinity of Gulf Coast salt structures (Hanor and Sassen, 1990; Bruno and Hanor, 2003; Steen et al., 2011). The shallowest regime has normal marine salinity levels (35 g/L) and is hydrostatically pressured. The deepest regime also has near marine salinity values, but is overpressured and is largely shale-dominated. The middle regime is sand-dominated, hydrostatically pressured, and contains formation waters with elevated salinity values (up to 350 g/L). Because of the elevated saline levels in the middle regime, fluid flow occurs in part as a result of density variation, with the more dense brines flowing down-dip away from the salt structure (figure 1).

Density gradients and thermohaline convection caused by temperature and salinity variations near salt structures are known to be a drive for fluid flow downward from the source of the subsurface brines (Evans et al., 1991; Bruno and Hanor, 2003; Steen et al., 2011; Richards, 2013)(figure 1). Fluid expulsion upwards along faults from the deepest overpressured regime, due to a high hydraulic gradient is another driving mechanism for fluid flow near Gulf Coast salt structures (Bennett and Hanor, 1987; Ranganathan and Hanor, 1989; Hanor and Sassen, 1990; Lin and Nunn, 1997). Figure 2 depicts this process where geopressured fluids migrate vertically

upward along faults near salt, and then move laterally outwards within the hydrostatically pressured regime on the flank of Welsh Dome, an onshore Louisiana salt dome.

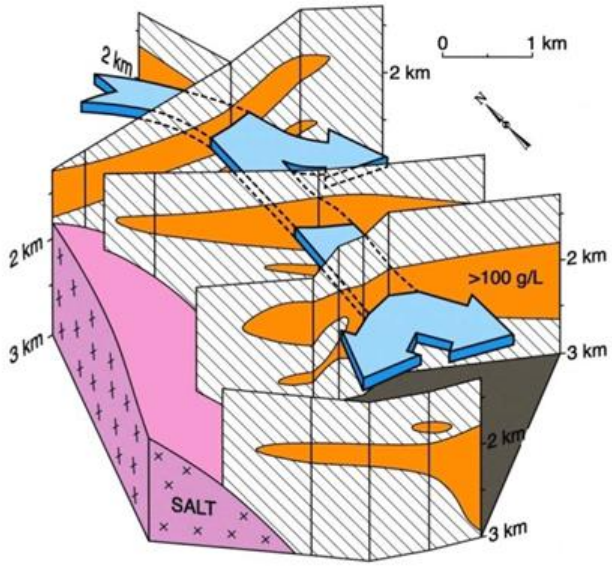

Figure 1: Fence diagram from Bay Marchand, in offshore Louisiana, that shows saline plume (blue arrows) originating at top of salt structure and migrating downdip through sandy intervals (Bruno and Hanor, 2003)

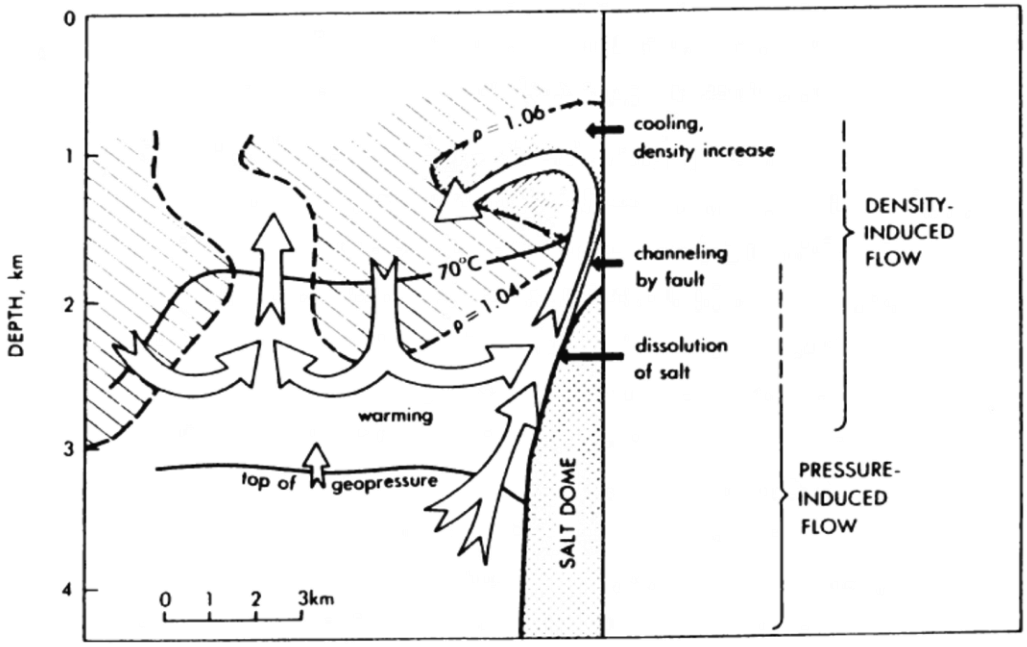

Figure 2: Diagram from Welsh dome, an onshore Louisiana salt dome, that shows large-scale fluid migration as a result of variations in hydraulic head (Bennett and Hanor, 1987)

Bruno and Hanor (2003) also determined that the distribution of saline brines near the Bay Marchand salt structure was controlled largely by the lithology. They concluded that saline plumes preferentially migrated through sand-dominated sections, since sand is more permeable than shale. Bennett and Hanor (1987) and Lin and Nunn (1997) concluded that formation waters can also migrate along fault planes in the vicinity of Gulf Coast salt structures. Their research showed that overpressured formation waters with marine salinities expulsed upwards along fault planes into overlying hydrostatically pressured reservoirs. It has long been recognized that faults surrounding Gulf salt structures are conduits to the upward migration of hydrocarbons as well, where hydrocarbon reservoirs are sometimes charged by hydrocarbons that have vertically migrated thousands of meters from deeper source (Galloway, 2009). Fault planes have also been shown to be conduits for marine and shallow formation waters migrating downward and causing the dissolution of salt, and thus, elevating the salinity of the local pore water (Bruno and Hanor, 2003; Richards, 2013). Alternatively, Bruno and Hanor (2003), Steen et al.(2011), and Richards (2013) found faults to be barriers to the flow of hypersaline formation waters that were migrating perpendicular to the fault plane through sandy sections down dip. Figure 3 shows the offset of salinity values of formation waters located on the southwest flank of the Bay Marchand salt structure, offshore Louisiana. Bense and Person (2006) concluded that because the permeability of faults is controlled by multiple factors which can vary through time, faults can have dual behavior, acting both as conduits and impediments to flow at different times and/or different depths. Some factors that control the permeability and behavior of faults within fluid flow systems are the burial depth, fault throw, and secondary mineralization along the fault plane (Bense and Person, 2006).

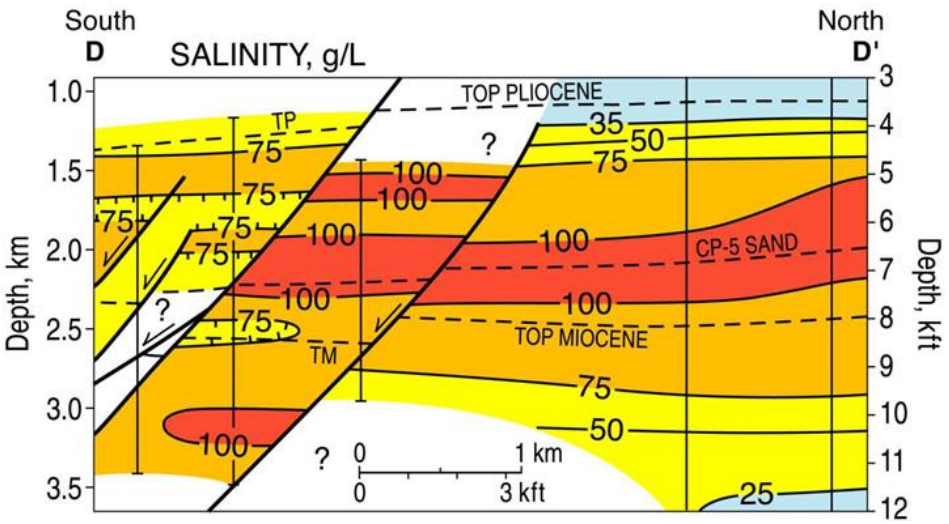

Figure 3: Cross section from Bay Marchand, offshore Louisiana, demonstrating fluid compartmentalization by faults (Bruno and Hanor, 2003)

The main objective of this study was to identify structural, thermal, and lithologic controls on the distribution of formation waters. One goal was to identify fault compartmentalization as seen by Bruno and Hanor (2003) and Steen et al.(2011). The 3D seismic survey that Steen et al.(2011) used was not time-depth converted, so by converting the same seismic survey, this study aimed to more accurately image fault compartmentalization. Another goal of this research was testing the Bruno and Hanor (2003), Steen et al.(2011) and Richards (2013) hypothesis that saline brines preferentially migrate through sand-dominated sections by using a different method for calculating salinity. One final goal of this research was to potentially identify vertical migration of formation waters through temperature mapping, as was done by Richards (2013) at the crest of Bay Marchand, by Bennett and Hanor (1987) at Welsh dome, and Lin and Nunn (1997) at Eugene island. Steen et al.(2011) did temperature mapping in the same study area, and did not identify any temperature anomalies, but by using better data coverage, this research aimed to more accurately map temperature for this study area. The exact location of this study area, the well identities, and location and details on the 3D seismic survey are proprietary and therefore cannot be identified. The 3D seismic survey was used to map the complex faulting and the location of salt within the study area. Digital well logs were used to

calculate salinity values continuously versus depth. Bottom hole temperatures from the headers of well logs were used to derive temperature gradients.

Study Area and Geologic Setting

The study area of this research is in the same location as Steen et al. (2011), as both studies used the same seismic survey; however, the two studies used different well data. Though the two studies used different well data, the approximate locations of the wells from both studies was within the same area (indicated by the inset box in figure 4). The study area is located on the continental shelf of offshore Louisiana in the Gulf of Mexico sedimentary basin. The 3D seismic survey used in the study encompasses 40 km² and well data are distributed across a 6.5 km² area in the southern portion of the survey (figures 4 and 5). The well depths used are 3000 ft to 14500 ft (1000 m to 4500 m) below sea level. The sediments at these depths are Pleistocene to Upper Miocene in age and overlie a large dome-like salt structure (Steen et al., 2011). The apex of the salt structure is located to the north of the study area.

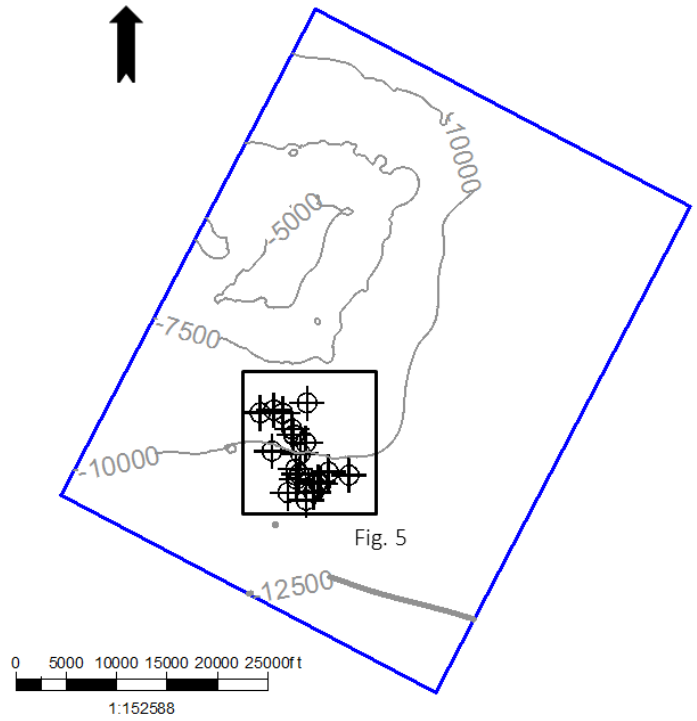

Figure 4: Bottom hole locations of the 21 wells used for salinity mapping in black, with top of salt contours in grey (ft subsea), outline of 15 mi² (40 km²) seismic survey in blue.

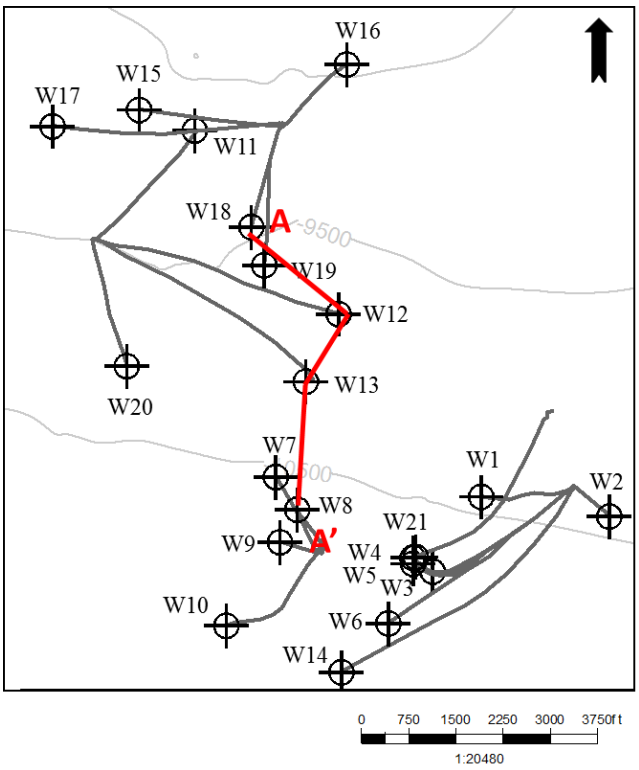

Figure 5: Inset of figure4. Bottom hole locations in black, well deviation paths in dark grey, cross section A-A' (figure 17) in red, and depth to salt contours in light grey (ft subsea)

The Gulf of Mexico sediment basin first started forming in the Late Triassic at the beginning of the breakup of Pangea. A massive salt formation, the Louann Salt, was deposited during the Triassic while there was a narrow rift valley between the Yucatan and North America. The sea transgressed into the rift valley multiple times as global sea level rose and fell throughout the Jurassic, which caused a thick sheet of salt to be deposited (Salvador, 1991). Clastic sedimentation during the Cenzoic caused differential loading on the Louann Salt. This rapid differential loading onto the salt and older muddy sediment, triggered build up of pressure in the muddy sections and diapirism of the Louann Salt to form numerous salt domes and structures along the entire Gulf Coast margin (figure 6). The geopressurization and salt diapirism in turn, caused structural deformation and strong pressure gradients between deeper and shallower sections of sediment. Since the Miocene, the shoreline on the Gulf Coast has

fluctuated across the area many times in response to the rates of sediment supply, eustasy, and subsidence, but the dominant movement of sediment has been seaward (Frey and Grimes, 1970; Galloway et al., 2000; Galloway, 2009). There are three gross sedimentary facies within the Gulf Coast Cenozoic sedimentary section which are represented in this study area: a massive sandstone facies of Pleistocene age, an interbedded sandstone and shale facies of Pliocene age, and a massive shale facies of Upper Miocene age (figure 7).

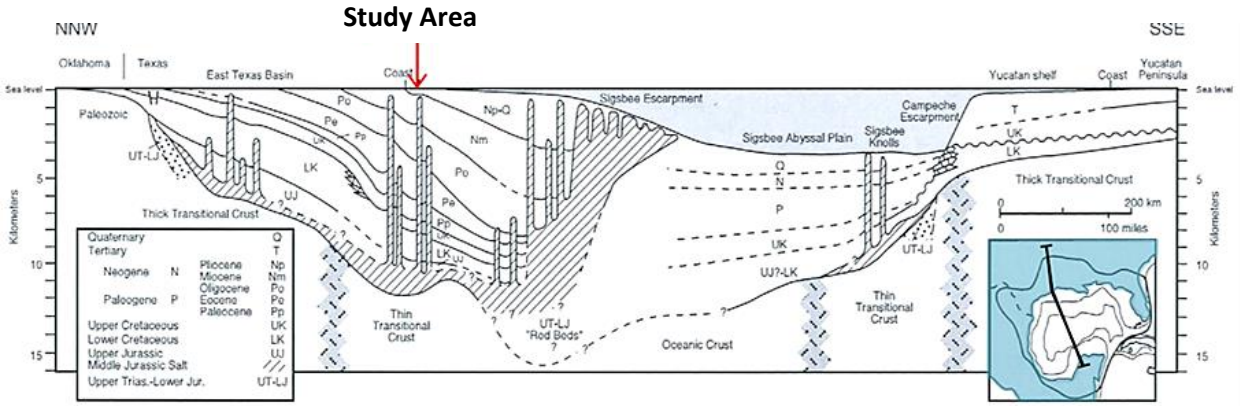

Figure 6: Diagrammatic cross section of Gulf of Mexico depicting Tertiary to Miocene sediments overlying Jurassic salt (Modified from Galloway et al., 1991)

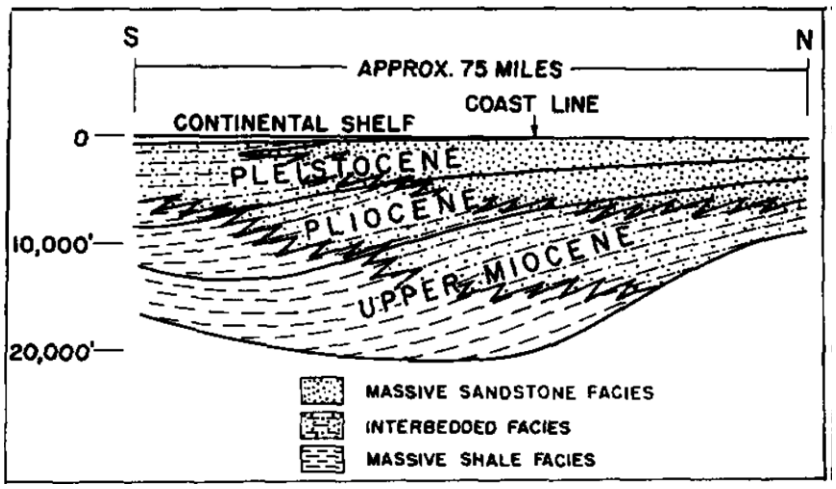

Figure 7: S-N cross section of South Louisiana showing the major lithologic facies of the Gulf Coast, study area approximately located where the coast line is indicated (Frey and Grimes, 1970)

Data and Techniques

Two sets of wireline log data were used in this study: the smaller set used for salinity mapping included 21 wells that had digital gamma ray and resistivity logs and covered a logged interval of 3200-1000 ft (1000-3500 m), the larger set of well log headers used for temperature mapping included 59 wells which had multiple bottom hole temperatures recorded (figure 8). A depth converted 3D seismic survey was also used.

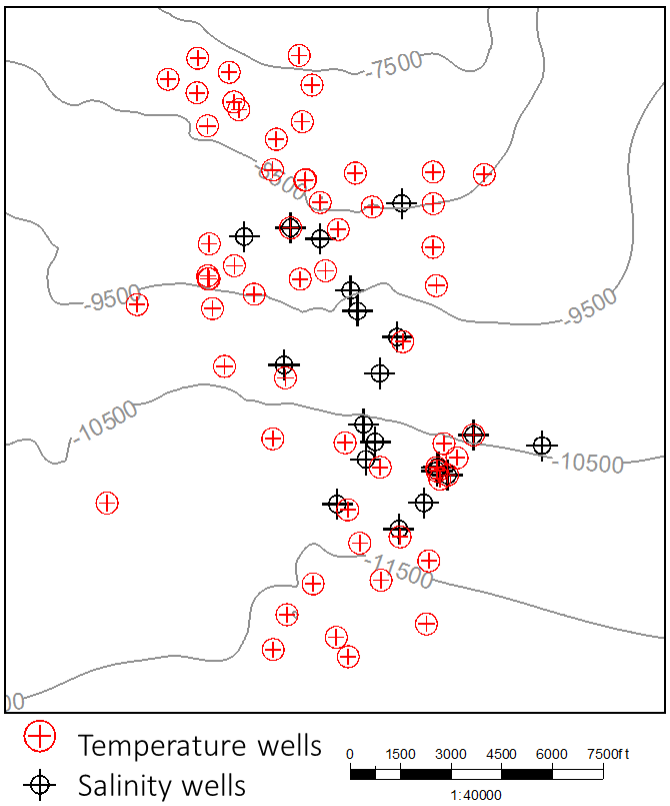

Figure 8: Bottom hole locations for two well sets with depth to salt contours (ft subsea). Notice that the temperature well set has a broader geographic distribution than the salinity well set

Seismic

In order to accurately interpret the stratigraphy and structure from the seismic survey and to accurately correlate well and seismic data, a time to depth conversion was necessary. The 3D seismic survey used in this study was depth converted by applying a constant linear velocity

derived from the sonic log values for 13 wells throughout the study area. Figure 9 shows the sonic values for the 13 wells versus depth. Several depth conversions were attempted by using several different velocity models derived estimations of velocity versus depth from sonic log data which included a velocity model with a single linear velocity trend for all depths, a velocity model with two different linear trends at two depth intervals, a velocity model with a linear trend of velocity at shallower depths and a constant velocity at deeper depths, a velocity model with multiple constant velocities, and a velocity model with one constant velocity for all depths. To determine which velocity model was the best fit for the depth conversion, the resulting depth to the top of salt was compared to published values of depth to salt for this study area, since biostratigraphy nor well top data was provided for the well logs and the top of salt is a clear amplitude that is easily interpreted from the seismic data. The velocity model that provided depths to salt comparable to published values was a constant velocity model of 8000 ft/s (2400 m/s) for all depths (figure 9).

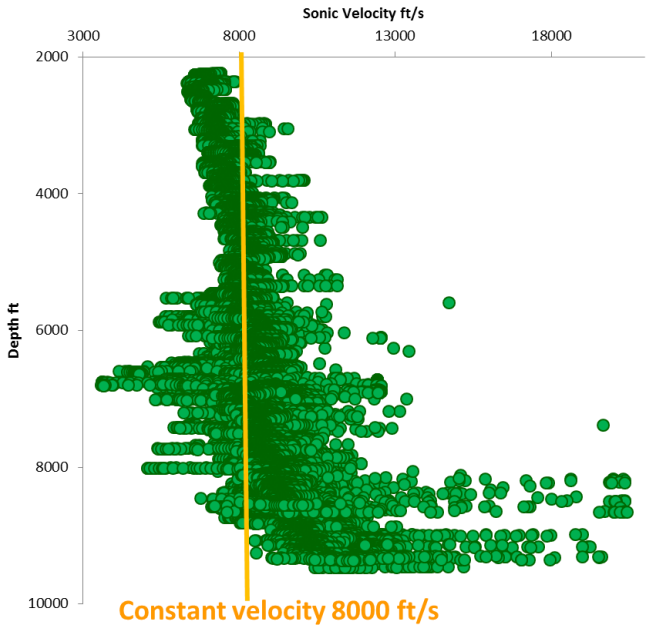

Figure 9: Sonic velocity plot for 13 wells in study area. Constant velocity of 2400 m/s used in depth conversion of seismic denoted in yellow.

Salinity

The Revil et al.(1998) method has been used in several studies to derive salinity from gamma logs, resistivity logs and clay and porosity parameters (Spears, 2000; Little, 2003; Hanor and Mercer, 2010; Daugherty 2012). This method is useful because it can be applied to both sands and shales for the entire continuous logged interval of the sediment section, as opposed to calculating salinity from spontaneous potential logs, which can only be done for discrete sandy intervals. Daugherty (2012) found there an error in Revil et al's (1998) description of their calculation methods for salinity, more specifically in the calculation of the cation exchange capacity value, therefore Daugherty's (2012) edits were applied to the salinity calculations.

The Revil et al.(1998) method uses gamma and resistivity logs to derive salinity, but other parameters are also required. The clay weight fraction of the study area is required to calculate the cation exchange capacity (CEC) of clay and the gamma ray level of pure shale (GR_{sh}), parameters which remove the effects of clays on the resistivity logs so that the resistivity logs only reflect the changes in resistivity due to changes in the pore water and not changes in lithology. No core analysis data were provided in this study, so the clay weight fraction values from the Revil et al.(1998) study (Table 1) at Eugene Island, offshore Louisiana were used to calculate a CEC value of 0.43246 and a GR_{sh} value of 162.5, as the Revil et al. (1998) study was done in a similar geologic setting and is in relative proximity to this study area. Because some sands in the study area contain hydrocarbons, the Waxman and Smits (1968) correction for hydrocarbons was applied to the Revil et al.(1998) method, so that the hydrocarbons' effect on resistivity logs was also removed (see Dougherty, 2012).

Table 1: Clay weight fraction, CEC, and GR_{sh} values from Revil et al. (1998) which were used in salinity calculations

% Mixed layer clays	% Illite	% Kaolonite	% Chlorite	CEC	GR_{sh}
64.5	1.75	15.5	18.25	0.43246	162.5

Porosity is another parameter required in the Revil et al. (1998) method of calculating salinity. Only one well had neutron and density porosity logs in this study and no core data was provided, so estimating porosity by another method was necessary to calculate salinity. Hanor (personal communication, 2014) collected porosity data from neutron porosity and density porosity logs across the northern offshore Gulf of Mexico. A coarse estimate for porosity could be derived for the wells in this study by extracting the linear equation for porosity versus depth from Hanor's (personal communication, 2014) neutron and density logs for wells across the northern Gulf of Mexico. Salinities calculated using porosity from neutron and density porosity logs from a well within the study area (but not included within the salinity well dataset because it was not proximal to faulting - location of well included in appendix 1) were calibrated against the salinities calculated using porosity from the linear porosity trend from Hanor (personal communication, 2014) (Appendix I). The two salinity curves were nearly identical with an average separation of 11 g/L, so the porosity estimation from the Hanor porosity trend was deemed acceptable for the purpose of this study. After collecting the necessary CEC, GR_{sh}, and porosity parameters, the Revil et al. (1998) algorithm was applied continuously for each of the 21 wells that had gamma and resistivity logs, and then a moving average was applied over 20 foot intervals to smooth the calculated salinity curve. Appendix II shows the calculated salinity curve without the moving average applied versus the salinity curve with the moving average applied for well 2 to demonstrate the smoothing effects of the moving average.

Temperature

Bottom hole temperature (BHT) values from 59 wells were used in temperature mapping (see figure 8 for well locations). Temperature values for temperature maps were derived from interpolation between bottom hole temperature (BHT) values taken from well log headers and the surface temperature. BHT values were corrected for the cooling effect associated with drilling mud by using the Kehle (1971) correction curve. Figure 10 shows all of the BHT readings used in temperature mapping versus their depths. The trend of BHT's reflects a temperature gradient of 13.4°F/kft (24.4°C/km), which is comparable to the average geothermal gradient of 13.7°F/kft (25°C/km) from Steen's (2010) well data in the same study area. Since bottom hole temperature values were taken at depths ranging from 3500 to 15000 ft SSTVD (1000-4500 m SSTVD), temperature maps were created at the top (6,000 ft (2000 m) SSTVD) and the base (10,000 ft (3000 m) SSTVD) of the logged interval with adequate data coverage (there are 33 BHT readings taken within 1500 ft of 3000 ft SSTVD, and 89 BHT readings taken within 1500 ft of 10,000 ft SSTVD). In order to generate maps at those two depths, it was necessary to calculate the local geothermal gradient for each well and then interpolate to 6,000 and 10,000 ft SSTVD. Every well had at least two BHT readings but most of the readings were taken within a few hundred feet of each other. Since the distance between BHT readings is one to two orders of magnitude smaller than their depths, interpolating between them would not give an accurate representation of the geothermal gradient for the entire well. Therefore, when the BHT's were within a few hundred feet of each other, they were projected to the surface temperature of 68°F (20°C) (Li et al., 1997) to get a more accurate geothermal gradient to interpolate to the two mapped depths (figure 11). Figure 12 is a plot of the geostatic ratio for the depths where BHT readings were taken. From this graph you can see that the top of overpressure is between 8000 ft and 11500 ft SSTVD in the study area. Although figure 10 does not reflect an

obvious change in geothermal gradient below the top of overpressure, the overpressured zone in the Gulf has been known to have elevated temperatures due to the low thermal conductivity of the excess amount of interstitial fluids compared with that of the rock grains (Lewis and Rose, 1970); to account for this possibility in the study area, only BHT values above 8,000 ft were used in construction of the 6,000 ft temperature map and BHT values below 8,000 ft were used in construction of the 10,000 ft temperature map. It is also important to note that BHT values have an error value of ±2-4°F (Blackwell and Richards, 2004) due to tool, human, and correction for cooling by mud circulationerror.

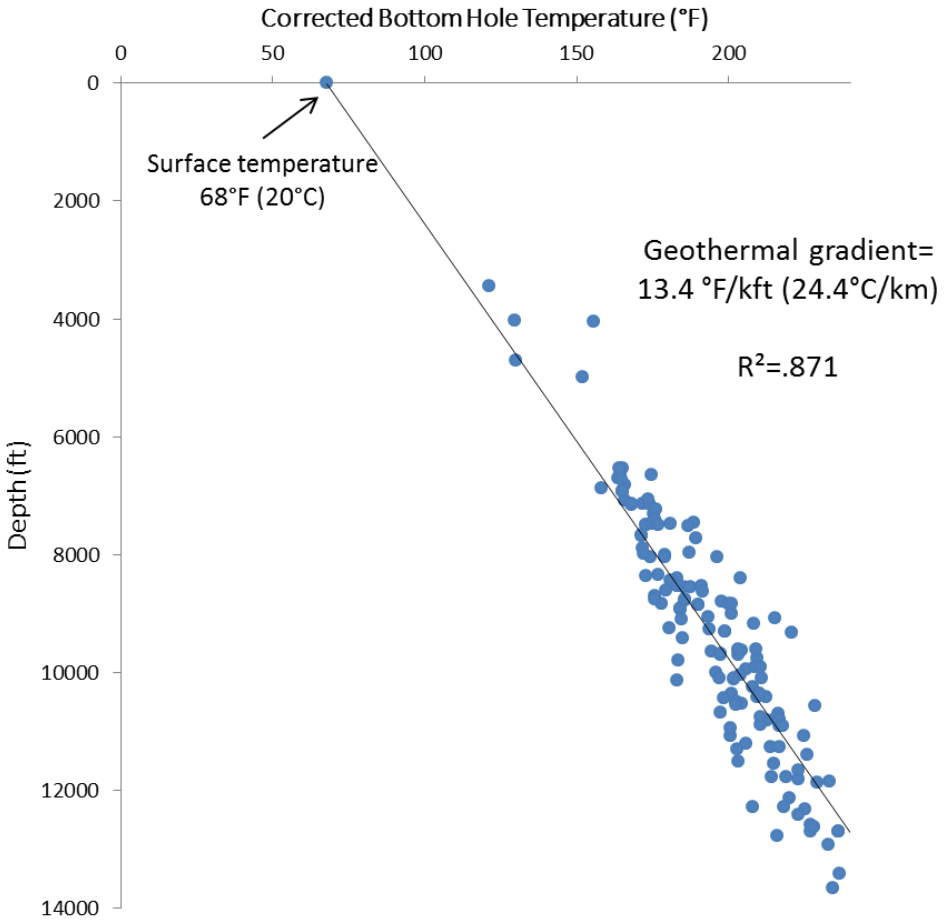

Figure 10: Graph of corrected bottom hole temperature values for wells in temperature well set, with surface temperature plotted at 68°F (20°C). Note that there is no obvious change in the geothermal gradient at depth.

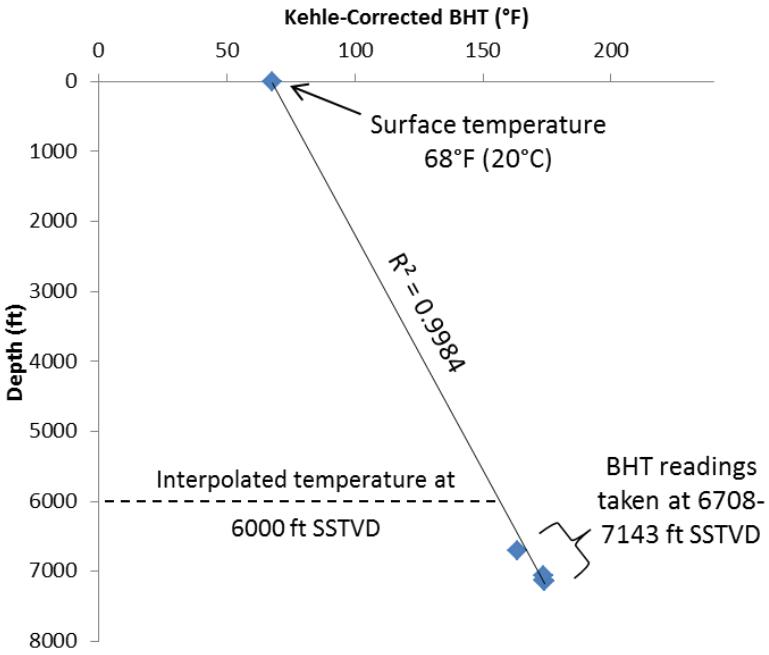

Figure 11: Example of the method for interpolating the temperature value at 6000 ft SSTVD by projecting multiple BHT values to the surface. Note that the difference in depths between the shallowest and deepest BHT readings is 435 ft, an order of magnitude smaller than the depth of readings

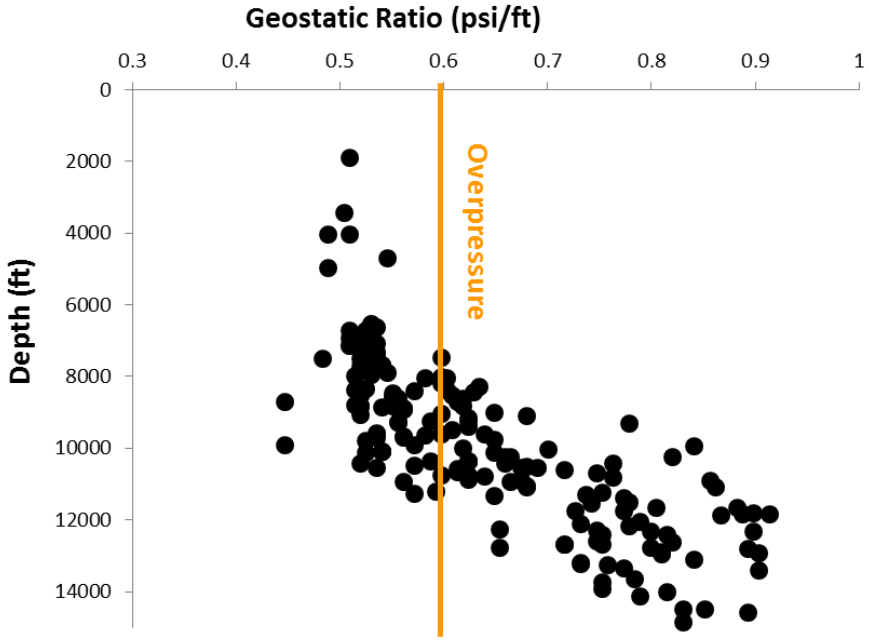

Figure 12: Geostatic ratio of bottom hole locations in temperature well set. Geostatic ratio values above .6 psi/ft are considered to be overpressured, so the top of overpressured sediments range from 8500- 11500 ft SSTVD.

Results

Structure

Interpretation of the seismic data showed that there is a highly complex system of extensional faults surrounding the diapiric salt structure in the central portion of the seismic survey. There are two sets of faults seen: the main set has longer faults that dip to the southwest, and the other set has smaller faults that are antithetic to the larger set and dip to the northeast. All of the seismic lines west of figure 13 have data gaps, where sections of the the seismic lines are not present. Figure 13 shows the westernmost complete seismic line with interpretations for faults in black and the top of salt in dashed red. The two biggest faults in the seismic line are crestal growth faults located on the top of the salt structure and extend all the way up to the seafloor, they dip in opposite directions to the southwest and northeast. There are five additional small faults on the flanks of the salt that step outwards from the crest of the salt and also dip to the southwest and northeast. Figure 14 shows an interpreted seismic line located in the center of the study area. Here the salt does not reach as high as in figure 13, but the southwest-dipping larger crestal growth faults extends from the top of the salt structure to the sea floor. There are also four smaller additional faults to the west of the major crestal fault, three of which dip to the southwest, and one to the northeast. Figure 15 is the easternmost complete interpreted seismic line (all seismic lines to the east of this line have sections missing)). Here the salt is deeper than the resolvable seismic data, and there are two southwest-dipping larger faults which extend from the bottom of the seismic line to the seafloor. There are also five small faults northeast of the larger faults, and one smaller fault between the two larger faults. There is extensive complex faulting throughout the entire seismic volume, however, the majority of the faults throughout the study area have offsets of less than 100 ft (30 m).

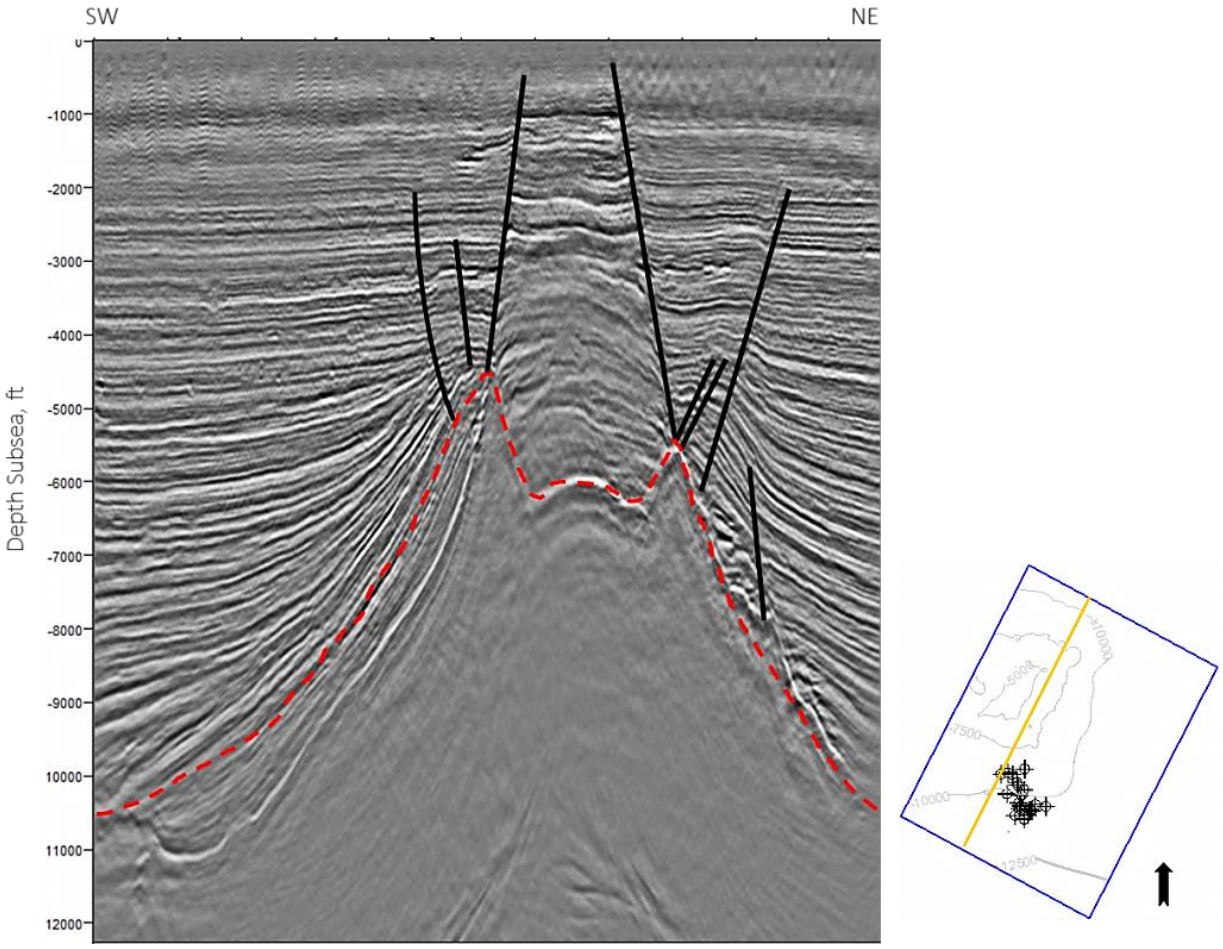

Figure 13: Two large crestal growth faults with 5 smaller faults on the flanks of the salt structure. Length of seismic line approximately 11 mi (18 km)

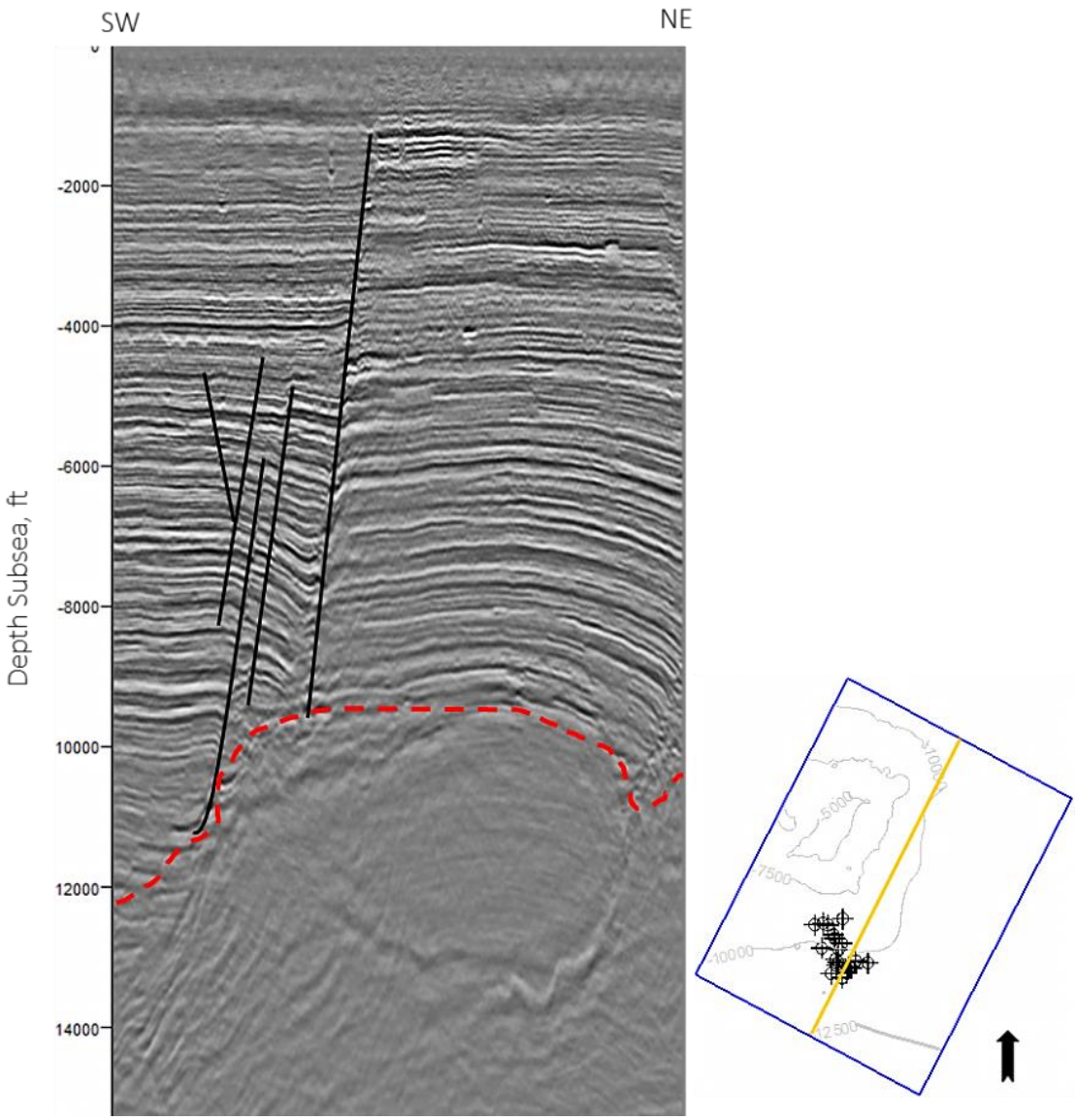

Figure 14: One crestal growth fault with 3 smaller synthetic faults. Length of seismic line approximately 11 mi (18 km)

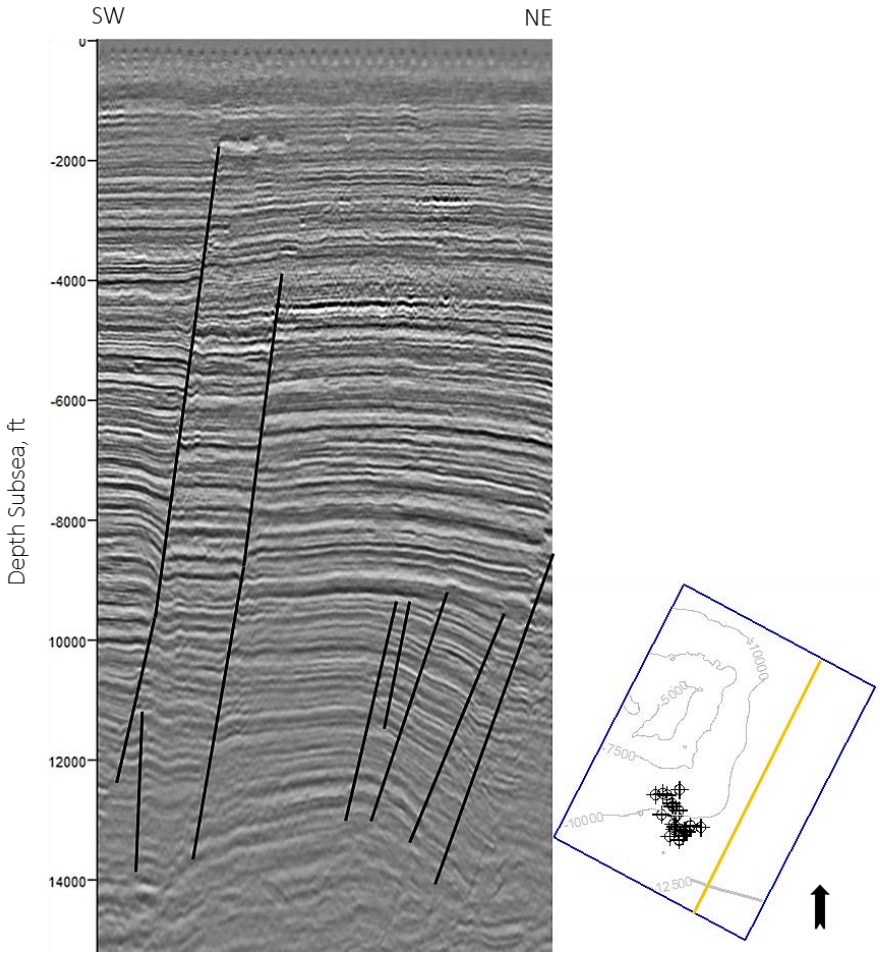

Figure 15: Two larger faults and 5 smaller step-like faults to the northeast. Length of seismic line approximately 11 mi (18 km)

Temperature

Two temperature maps were created for the top and base of the logged interval where there was adequate data coverage at 6000 ft (2000 m) SSTVD and 10,000 ft (3000 m) SSTVD. A natural neighbor gridding method was used in the program Surfer to generate the contour maps. Figure 16 is the temperature map at 6,000 ft SSTVD. Temperatures at this depth range from 144°F (21°C) to 166°F (74°C) and in general, the northwestern portion of the map is warmer than the southern portion. There is a large positive anomaly in the eastern portion of this map which contains readings from three wells that are about 15°F (8°C) warmer than the surrounding

area, which is larger than the standard error in BHT values. Figure 17 is the temperature map at 10,000 ft SSTVD. Temperatures at this depth range from 186°F (86°C) to 220°F (104°C). In general, the western portion of the map is warmer than the eastern portion. There is a small anomaly on the eastern edge of the map that represents two wells that are about 6°F (3°C) warmer than the surrounding area, and three wells in the center of the map are anonymously 4°F (2°C) warmer than their surroundings. Both of these anomalies are approximately the same size as the error in BHT values.

Salinity

Pore water salinities were calculated continuously for the 21 wells that had gamma and resistivity curves. Figure 18 is an example of one of the salinity curves shown against its gamma ray curve to demonstrate the variation of salinity with lithology (see appendix 2 for all salinity curves). Overall, two of the three established Gulf Coast hydrologic regimes could be identified from the 21 salinity and gamma curves, along with their pressure data: the middle regime (3200 - 8200 ft/1000-2500 m) has the highest salinity values ranging from 100 g/L to 250 g/L and is sand-dominated; the deepest regime (>8200 ft/2500 m) has lower salinity values of 30 g/L to 100 g/L and lies in a shale-dominated zone (figure 19). Steen et al. (2011) utilized shallower logs than those used in this study to determine that the shallowest, normal-saline, shale-dominated regime was at depths <3200 ft (1000 m) subsea in this study area. The shallowest logged depth in the well set used for salinity calculations is 3200 ft (1000 m) so the shallowest regime likely lies just above the logged depths used in this study; therefore, the boundary between the shallow and middle regime in the following figures was an estimation based on Steen et al.'s (2011) interpretations.

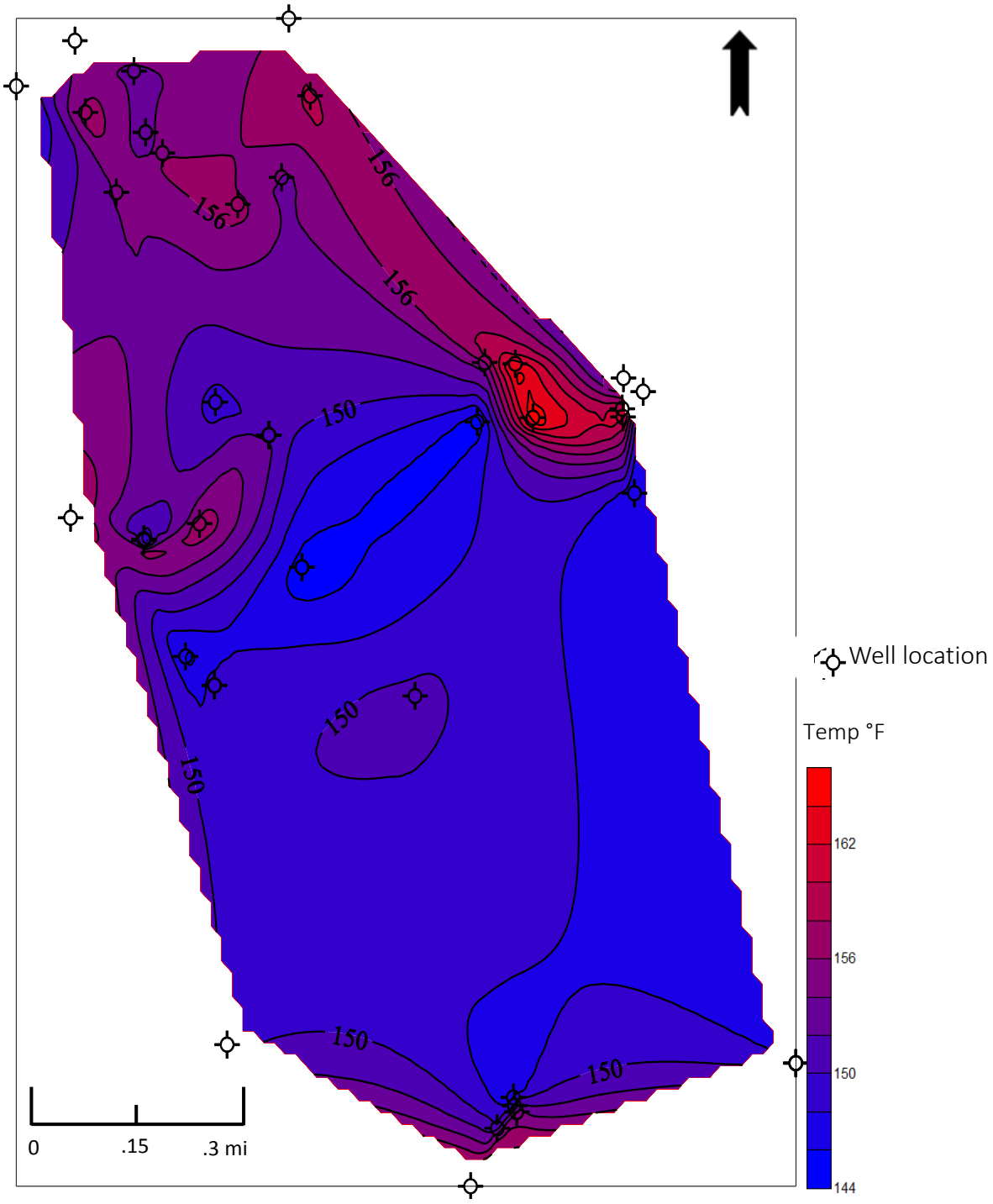

Figure 16: Temperature map at 6000 ft (2000 m) SSTVD. Crest of salt structure located to the north of map.

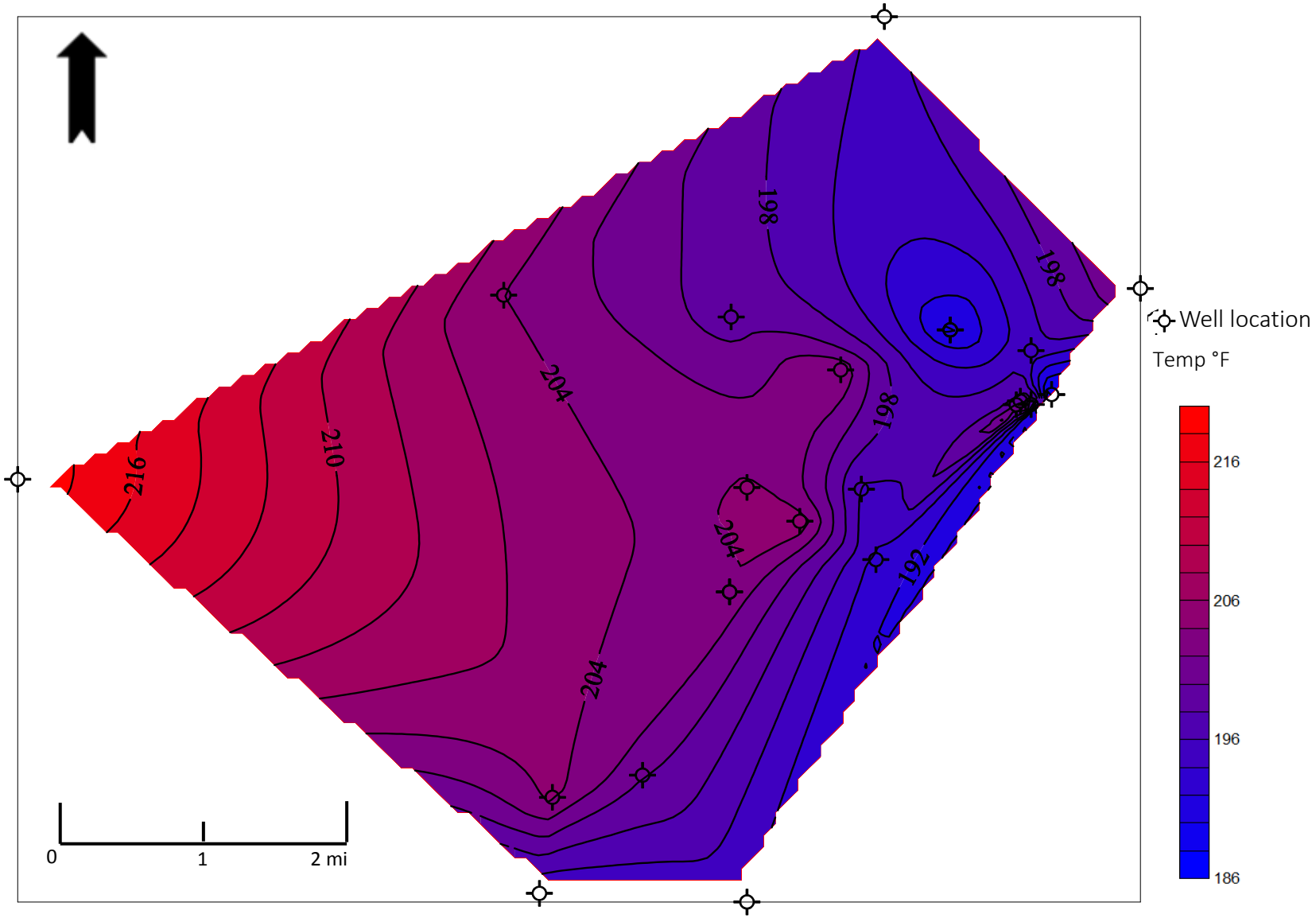

Figure 17: Temperature map at 10,000 ft (3000 m) SSTVD. Crest of salt structure located to the northwest of map

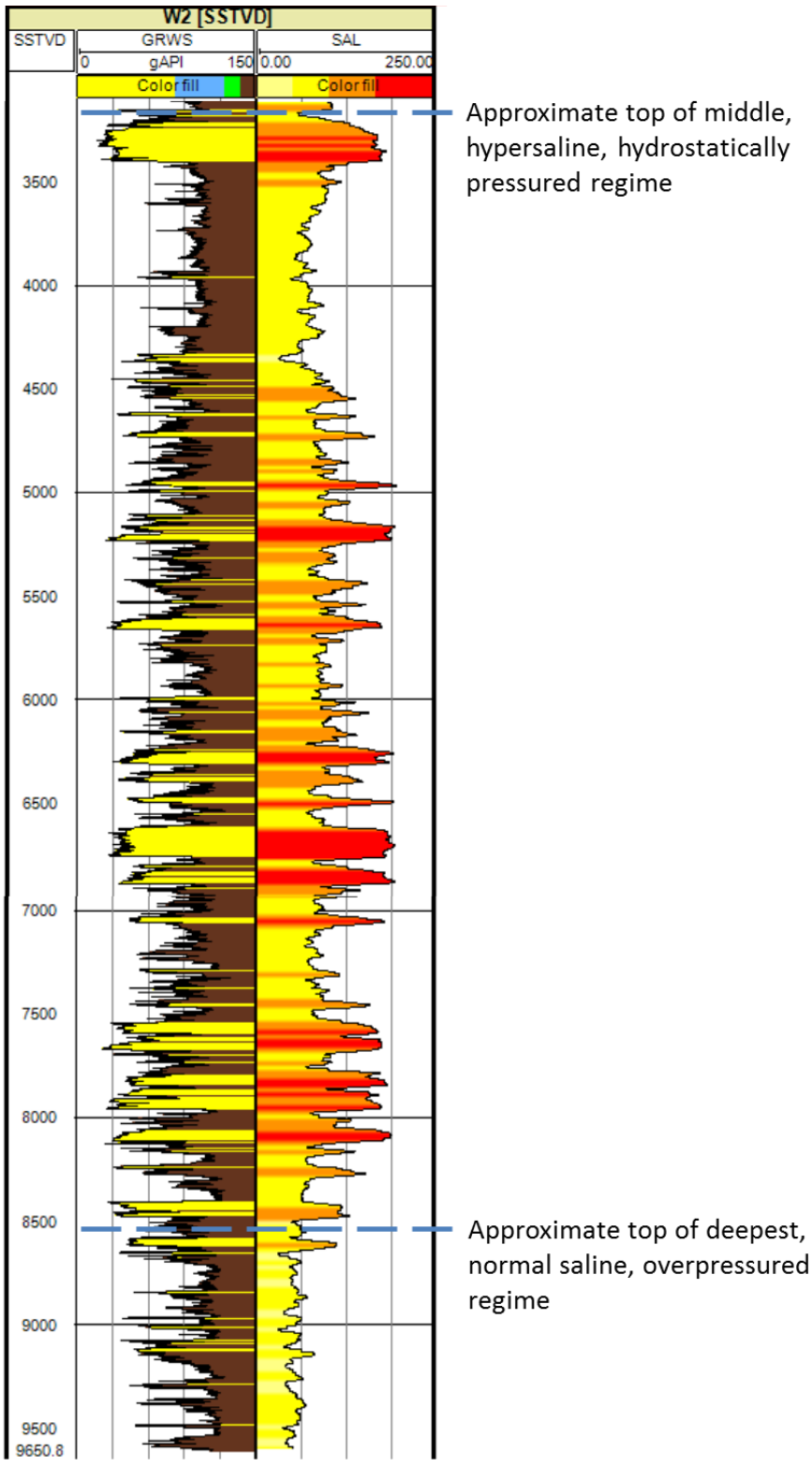

Figure 18: Gamma ray and salinity curves for well W2. Salinity curve has a moving average applied over 20 ft interval for smoothing. Lithologic curve fill for gamma ray curve where sand is yellow and shale is brown. Pressure (mud weight) data were not provided for this well so boundaries between regimes were determined by lithology, salinity values and Steen et al. (2011).

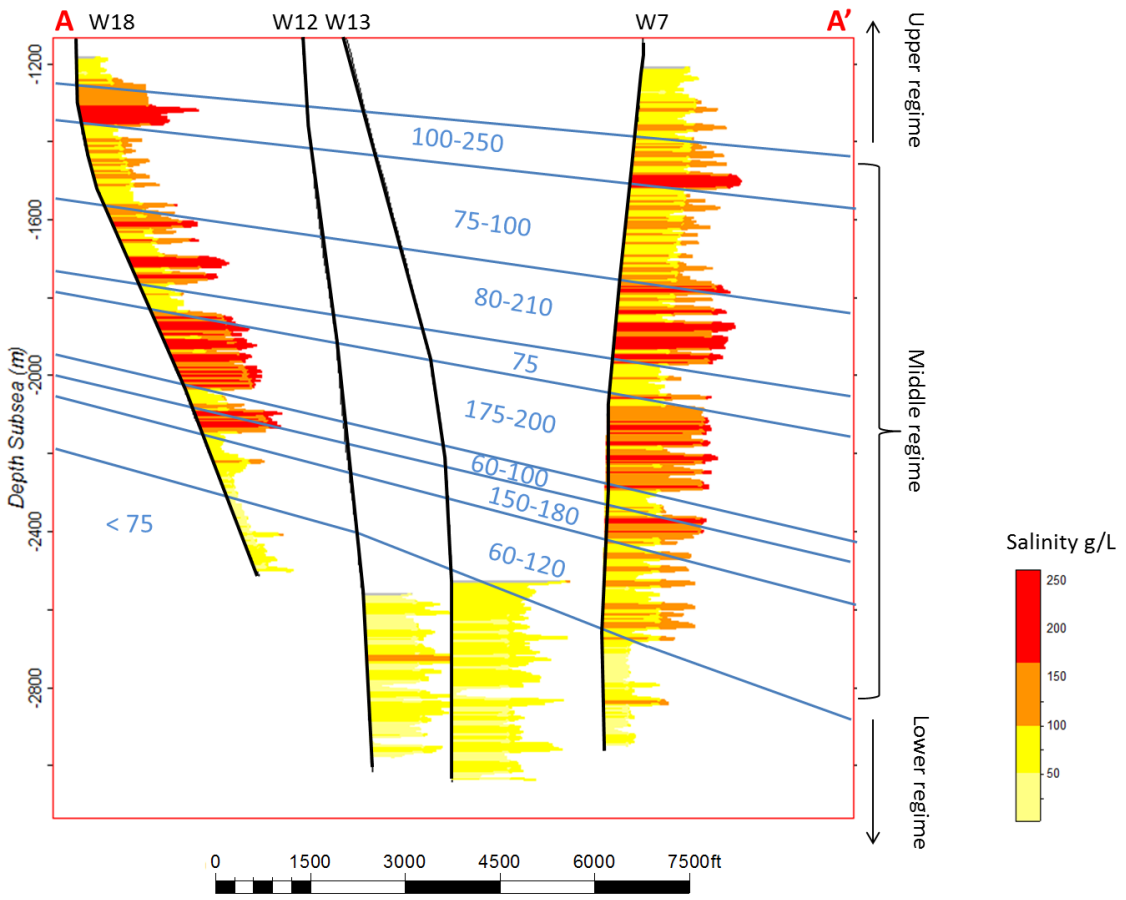

Figure 19: N-S cross section of salinity (location of cross section shown in figure 3). Salinity contours in blue. Pressure (mud weight) data were not provided for these wells so boundaries between regimes were determined by lithology, salinity values and Steen et al. (2011)

Two salinity maps were also created at 6000 and 10,000 ft SSTVD. Because salinity was only calculated in 21 total wells of varying depth ranges, the 6000 ft salinity map only contains 8 data points, and the 10,000 ft salinity map only contains 9 data points; both maps covered a smaller area than their respective temperature maps. A natural neighbor gridding method using Surfer was used to contour the salinity maps. The salinity map at 6000 ft (figure 20) ranges in salinity values from 65 to 130 g/L, and in general, shows salinity increasing from the southwest to the northeast. The salinity map at 10,000 ft(figure 21) has much lower salinity values and range from 40 to 79 g/L. There are two salinity peaks in the southwestern and eastern corners that are about 30 g/L greater than the salinity values in the northern and southern corners.

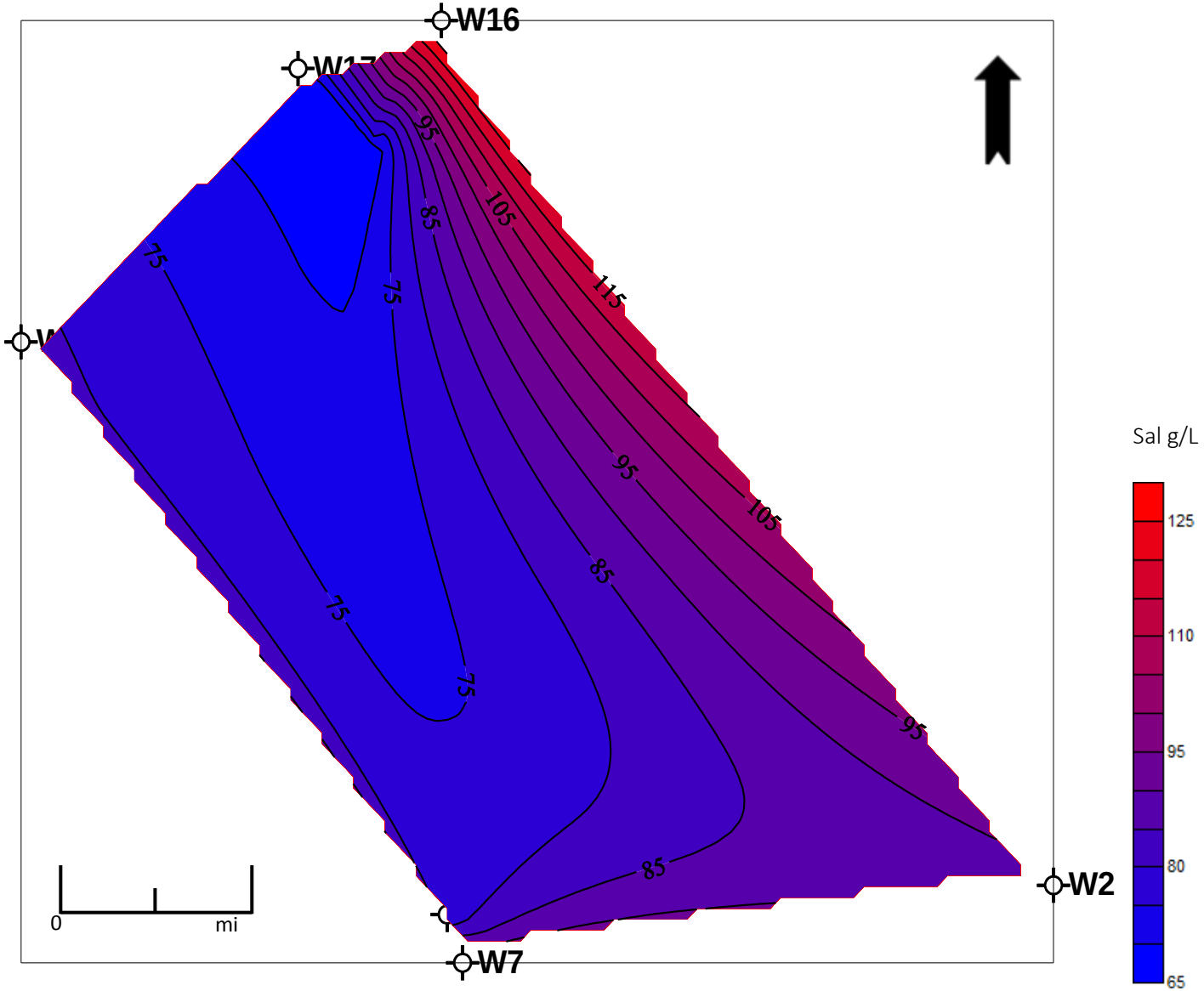

Figure 20: Salinity map at 6000 ft (2000 m) SSTVD. Well locations indicated in black

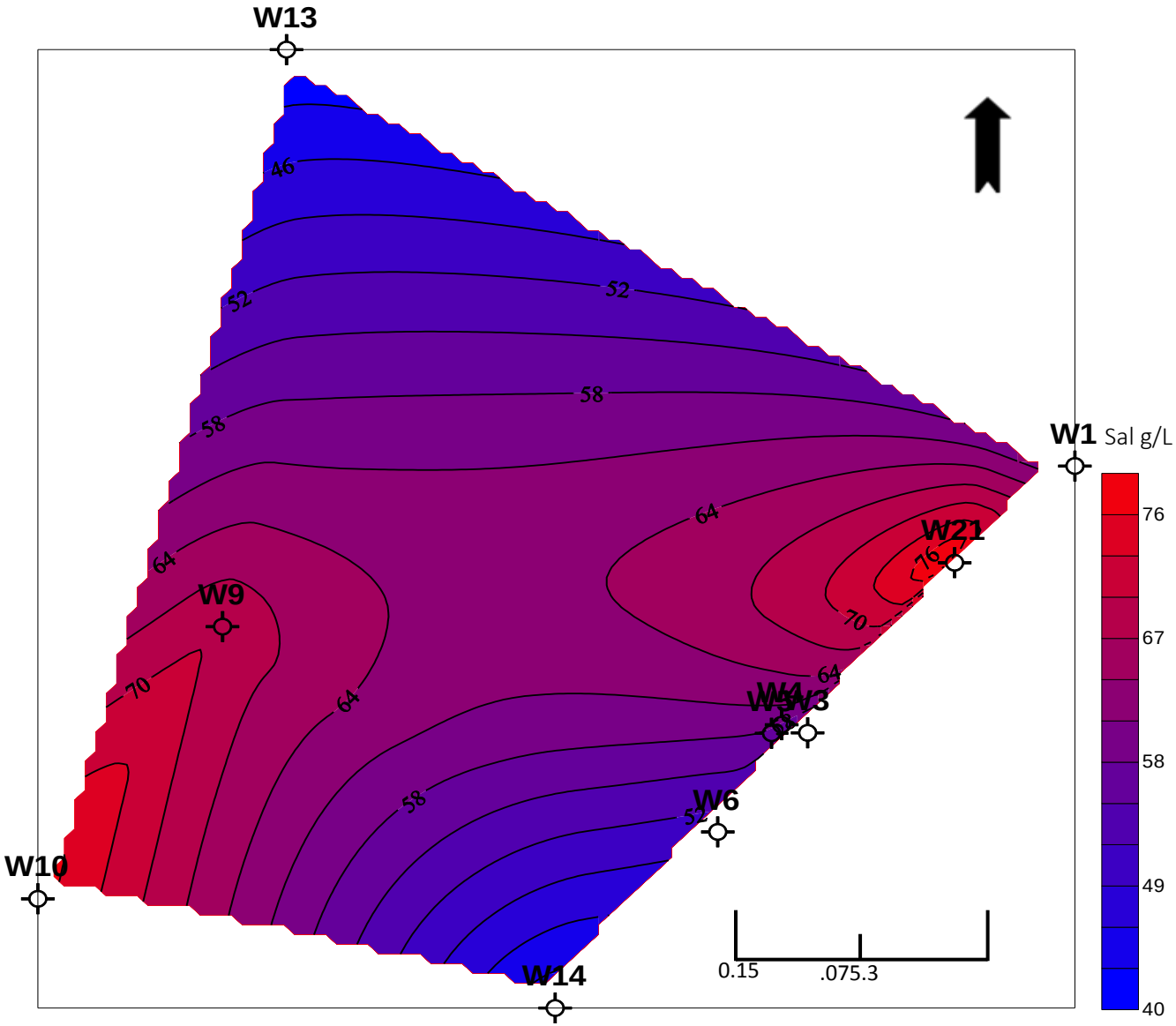

Figure 21: Salinity map at 10,000 ft (3000 m) SSTVD. Well locations indicated in black

Because pore water salinities were calculated continuously for the wells with gamma ray and resistivity curves, they could be displayed graphically in 3D along with the seismic interpretations of faults. This visualization technique provides a method for examining possible offset and compartmentalization of saline brines by faults. Figures 22 and 23 show two locations within the study area where the salinity values are offset/compartmentalized by faults. Figure 22 shows salinity values that are offset about 500 ft (150 m) by a fault. Figure 23 shows the offset of salinity values in wells W21,W6, and W14 by about 500 ft (150 m) and 750 ft (230 m). Also, W21 has salinity values about 50 g/L higher than the other two wells in sandy sections.

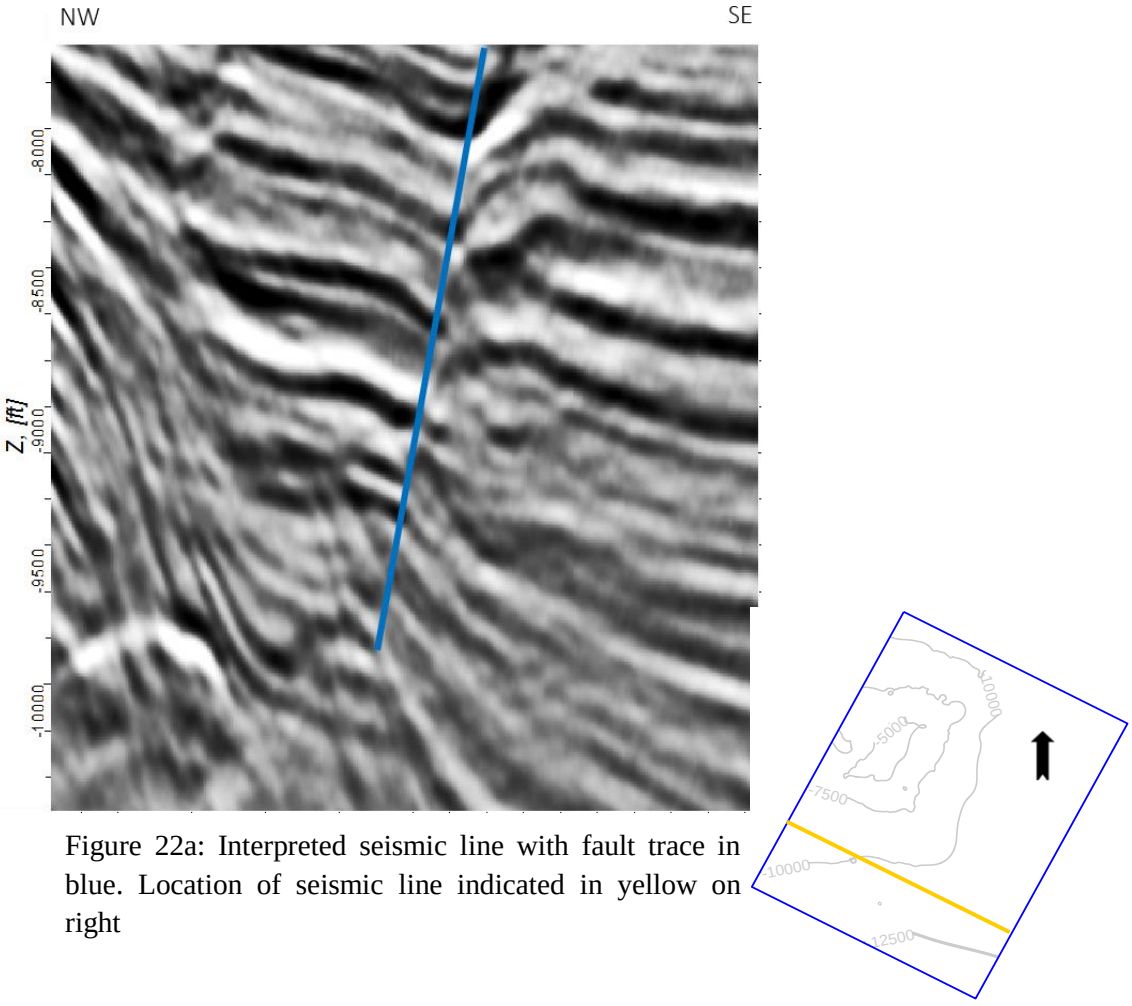

Figure 22a: Interpreted seismic line with fault trace in blue. Location of seismic line indicated in yellow on right

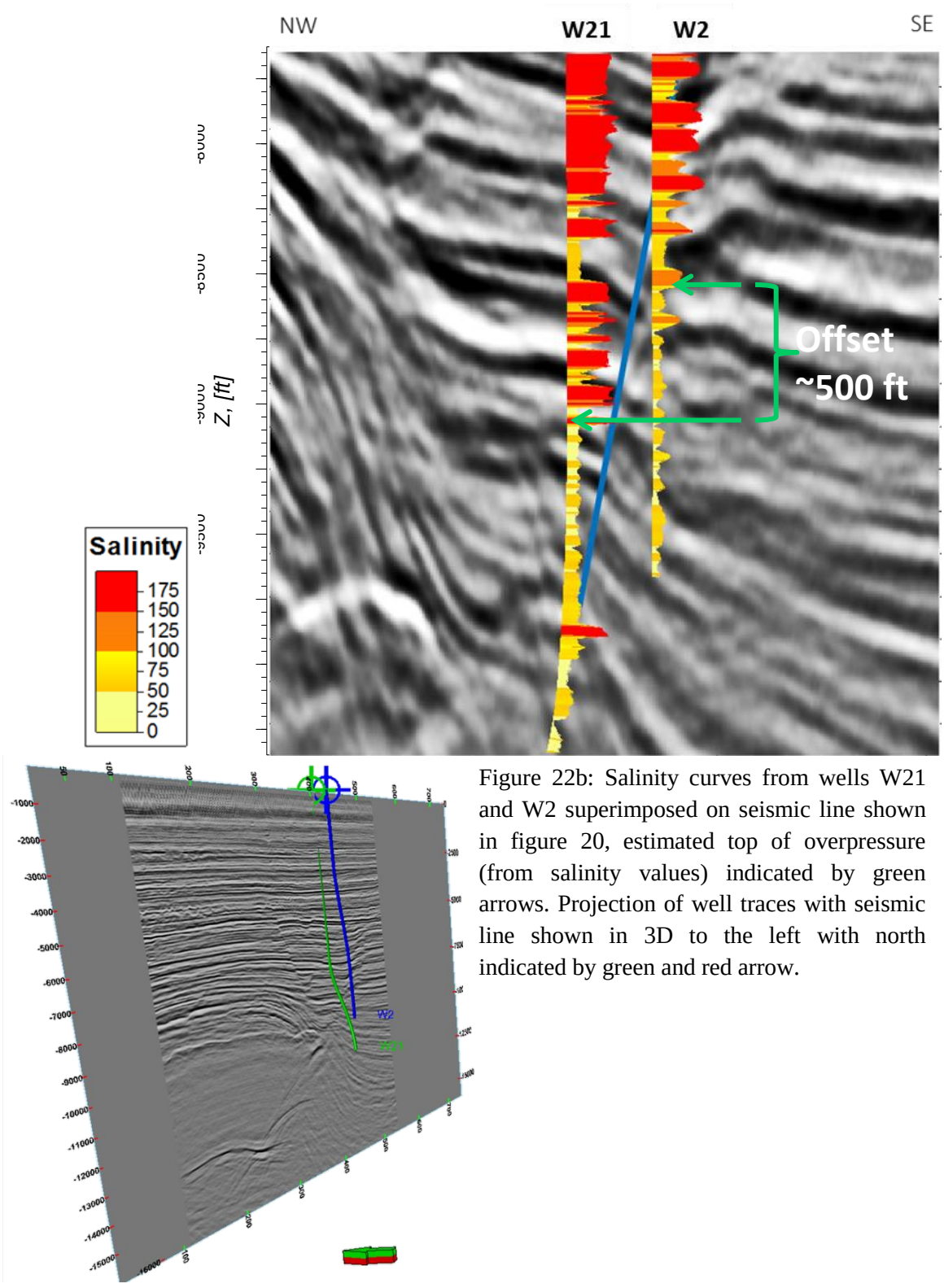

Figure 22b: Salinity curves from wells W21 and W2 superimposed on seismic line shown in figure 20, estimated top of overpressure (from salinity values) indicated by green arrows. Projection of well traces with seismic line shown in 3D to the left with north indicated by green and red arrow.

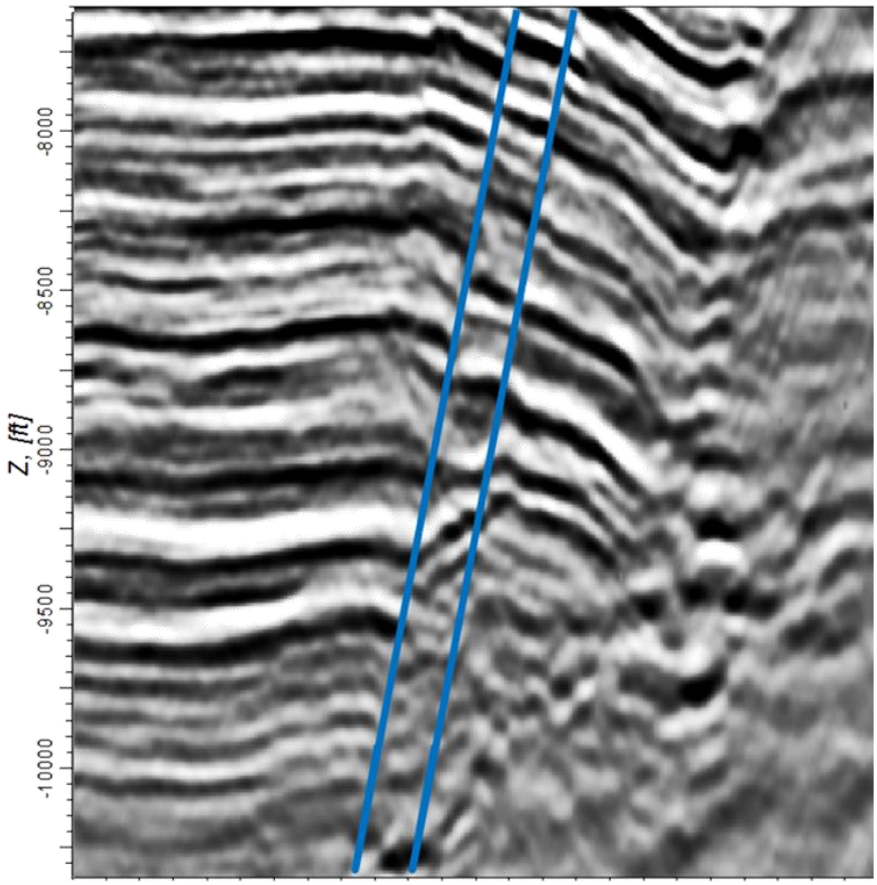

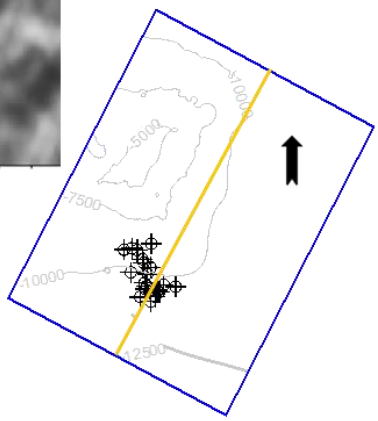

Figure 23a: Interpreted seismic line with fault traces in blue. Location of seismic line indicated in yellow on right

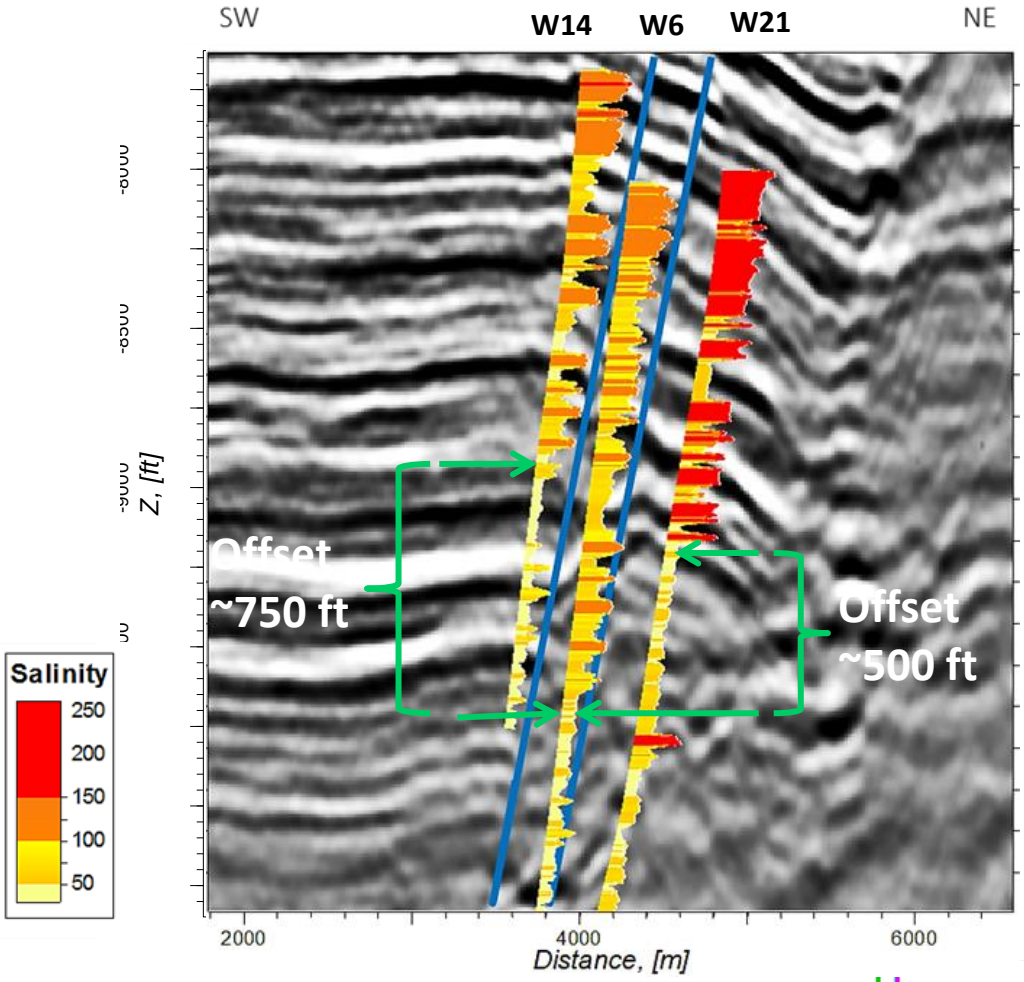

Figure 23b: Salinity curves from wells W21, W6, and W14 superimposed on seismic line shown in figure 23a, with estimated top of overpressure (from salinity values) shown by green arrows. Projection of well traces with seismic line shown in 3D to the right with north indicated by green and red arrow.

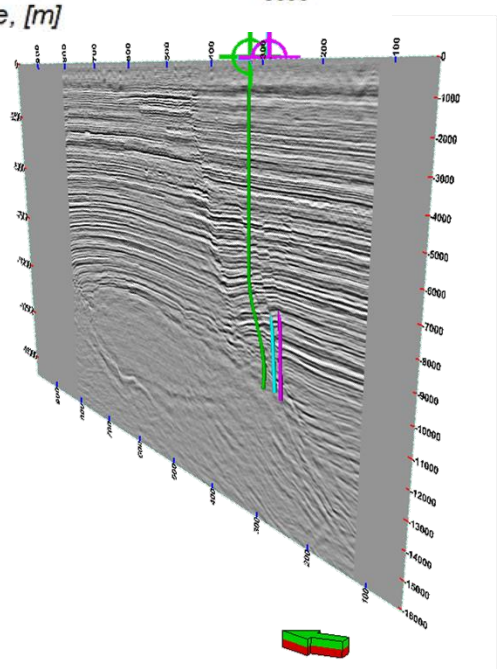

Discussion

Bruno and Hanor (2003), Steen et al. (2011), and Richards (2013) all hypothesized that lithology had a strong control on the migration pathways of saline formation waters, in that, dense brines preferentially migrated down dip through more sandy sections. However, each of their methods for calculating salinity could only be done in discrete sandy intervals. Two benefits of the Revil et al. (1998) method for calculating salinity are that it can be done in shales as well as sands, and that it can be done continuously on digital well logs. By comparing the continuous salinity curves generated from the Revil et al. (1998) method with their respective gamma ray logs, as in figure 16, one can see that the intervals with the lowest gamma ray readings (more sandy) have higher salinities and that the intervals with the highest gamma ray readings (more clay content) have a much lower salinity, and the thicker sand packages have higher salinities than thinner sands, as hypothesized by Bruno and Hanor (2003), Steen et al. (2011), and Richards (2013). This can be attributed to the sandy intervals having a higher permeability, which allow for the flow of hypersaline formation waters more easily than the shales that have a lower permeability.

The offset and compartmentalization of saline values by faults shown in figures 22 and 23 demonstrate that faults can be barriers to the flow of formation waters, as seen in this same study area by Steen et al. (2011) and at Bay Marchand by Bruno and Hanor (2003). However, in this study, these were the only two clear locations where this occurred, despite the highly complex faulting and continuous salinity data available for extended intervals. It is possible that some faults may impede flow rather than others because of the amount of offset or local lithology being offset; areas where a very shaly section are juxtaposed against a very sandy section are more likely to compartmentalize the formation waters than areas where the lithology

is similar on both sides of the fault (Jolley et al. 2010). The sealing capacity of the faults in these two locations may be higher also due to increased clay content within the fault (Jolley et al. 2010). Additional data from well logs in the vicinity of faults may offer additional insight into whether compartmentalization by a highly complex fault system is a more common occurrence above salt structures than seen in this study and as suggested by Bruno and Hanor (2003) and Steen et al. (2011).

Bruno and Hanor (2003) also hypothesized that the point of origin for the formation waters that were dissolving the Bay Marchand salt structure in offshore Louisiana to form saline plumes would likely be near the top of the structure. Richards (2013) investigated this hypothesis and located two negative temperature anomalies at the crest of the Bay Marchand salt structure that were interpreted as downward pathways for sea water which was the origin for the saline plumes mapped in Bruno and Hanor (2003). On the other hand, Bennett and Hanor (1987) and Lin and Nunn (1997) showed that in the vicinity of Gulf Coast salt structures, formation waters could also move upward from the deeper overpressured regime through faults and source reservoirs in the middle, highly saline regime. From the overlay of the fault polygons on top of the temperature maps in figures 24 and 25, it can be seen that the positive temperature anomalies roughly align with the faulted areas. Most notably, at 6000 ft SSTVD the very large temperature anomaly of +15°F aligns with the highly faulted area where several faults converge. The small temperature anomalies also align with the smaller fault polygons at 10,000 ft SSTVD as well. The temperature anomalies at both depths are beyond the standard error for BHT readings (±2-4°F) and all of the anomalies are centered on multiple wells, which demonstrate their validity. The overlay of the salinity maps onto the temperature maps and fault polygons in figures 26 and 27 shows that salinity increases from near-marine values towards warmer temperatures and

faulting, where it reaches hypersaline values of up to 150 g/L. Lin and Nunn's (1997) conclusion that formation waters can move upward from a deep overpressured zone into shallower sections and the three-dimensional view of the faults that intersect the two mapped depths may offer an explanation for why the faulted regions have higher temperatures and possibly higher salinities than surrounding areas. Figure 28 is a 3D image of interpreted faults and the top of salt horizon from the seismic data, with the horizontal temperature mapped depths cutting across a few of the faults (which are indicated in figures 24-27 by the black and grey polygons). From this figure, it can be seen that the three faults that intersect the 10,000 ft SSTVD map also intersect the 6000 ft SSTVD map. These three faults are the largest faults in the study area and reach to depths that are below seismic resolution, so it is difficult to interpret their geometry and their proximity to the salt structure at depth; however, the shallower, smaller faults that converge on the eastern portion of the 6000 ft SSTVD map clearly are juxtaposed against the flank of the salt structure. The three dimensional view of the structure combined with the temperature and salinity maps supports the conclusion that warmer, deep, overpressured formation waters that originally are located at the base of the faults and just above the top of the salt structure migrate upwards along the faults into the shallower, hydrostatically pressured regime to cause positive temperature anomalies; and since the base of the shallower faults that converge on the 6000 ft SSTVD map are in the immediate vicinity of the salt structure, fluids that move upwards along these faults come into direct contact with the salt, to cause the hypersaline values seen in the eastern portion of the 6000 ft SSTVD salinity map near the faulting in a hydrodynamic process that is similar to those seen at Welsh Dome by Bennett and Hanor (1987) and Ranganathan and Hanor (1989). Because the salinity values on the deeper salinity map are not as elevated as those in the shallower map, the faults that exist at this depth may not be located as close to salt as the

shallower ones. Other supporting evidence for upward migration of formation waters from depth is the difference in the magnitude of the temperature anomalies seen at the two depths. If water is migrating vertically over a period of time that does not allow for thermal equilibrium to be reached, the greater the distance that water migrates over a set period of time will lead to a greater anomaly in its temperature compared to its surroundings; therefore, the formation waters that cause the temperature anomaly at 6000 ft SSTVD may have migrated a further distance than those at 10,000 ft SSTVD, supporting the conclusion that formation waters are migrating vertically over a relatively short period of time to cause the temperature anomalies.

Because salinity values are near-marine in the areas at both depths where there is no faulting, the conclusion can be made that before the faults existed, the formation waters had near-marine salinities, and the faulting was a potential cause for the later migration of hypersaline fluids away from the salt structure into the currently hypersaline middle regime. A process by which this would occur is the onset of salt diapirism: before the salt diapir formed, there was no faulting and formation waters at all depths in this study area were near-marine, later, as the salt began to move upwards, growth faults formed which allowed for the migration of fluids upwards from the shale-dominated overpressured regime. On the other hand, the two locations where faults offset salinity values in this study and in Steen et al. (2011) indicate that those specific faults must have formed after the hypersaline formation waters were in place within the middle regime. It is likely that since the salt is currently still migrating upwards, there is continued faulting surrounding the structure. This can offer the interpretation that hypersaline waters were put into place by older fault activity, and continued faulting then offset those saline plumes by younger faults.

Steen et al. (2011) did not find evidence for upwards vertical migration of fluids through faults. The study perhaps did not find evidence of this process because there was no temperature anomalies present in their temperature mapping. Because Steen et al. (2011) had far fewer data points for the temperature mapping (20 wells compared to the 59 wells used in this study), which was done in fence sections, rather than depth slices, it is possible that the poor data coverage did not allow for an accurate representation of the three dimensional temperature model for this study area. Also, fault interpretations and well ties in Steen et al. (2011) from the seismic survey in time are likely not as accurate as the seismic interpretations and the well ties done in this study, which were done on time-depth converted seismic. This could also be why Steen et al. (2011) did not conclude that formation waters were migrating upwards along faults from depth into the hypersaline zone.

Two recent studies have utilized the Revil et. al. (1998) method to study the distribution of pore water salinity in the deep water Gulf of Mexico basin. Hanor and Mercer (2010) used well data to examine the pore water salinity distribution on a regional scale. They found that, with the exception of near seeps, pore water salinity in the upper 500 m of sediments was close to marine values of 35 g/l. However, pore water salinities of 100 g/l were common at depths of 2 km or greater. Hanor and Mercer (2010) also found evidence for lateral and downward movement of dense brines. As in this study, upward migration due to expulsion of overpressured fluids was locally important. However, Hanor and Mercer (2010) determined that compaction expulsion and diffusion were the primary controls on vertical migration. Daugherty (2012) looked at seismic, well, and core data in a Mississippi Canyon field. Daugherty (2012) found two hydrological regions in his study area: a shallow hydropressured region with near marine pore water values and a deeper geopressured region with salinities of 100 g/l or higher.

Daugherty (2012) found upward migration of overpressured waters through faults, as seen in this study, to be a dominant flow mechanism near salt structures. Daugherty (2012) also identified down dip migration of dense brines as another flow mechanism present, also seen at Bay Marchand by Bruno and Hanor (2003) and Steen et al. (2011). Because there was no pressure (mud weight) data available for the salinity well set in this study, possible downdip migration of brines could not be identified here, so acquiring the well header data for those wells would be of interest.

There is clearly a limitation to the temperature and salinity maps in that they were only done in two discrete depths and that there is not ample data coverage for the maps, especially the salinity maps with 8 and 9 data points. The salinity maps were severely limited in data coverage, so they only cover a small portion of the area that is covered by the temperature maps. In turn, the interpretation that salinity increases towards faulting and the positive temperatures anomalies is not as obvious as the interpretations that stem from the temperature maps which have denser and broader data coverage. Also, because the seismic time to depth conversion was based on a simple constant velocity model, though the seismic velocity likely changes with depth, the interpretations of the faults from the seismic may not be the best representation of the actual geometry of the faults.

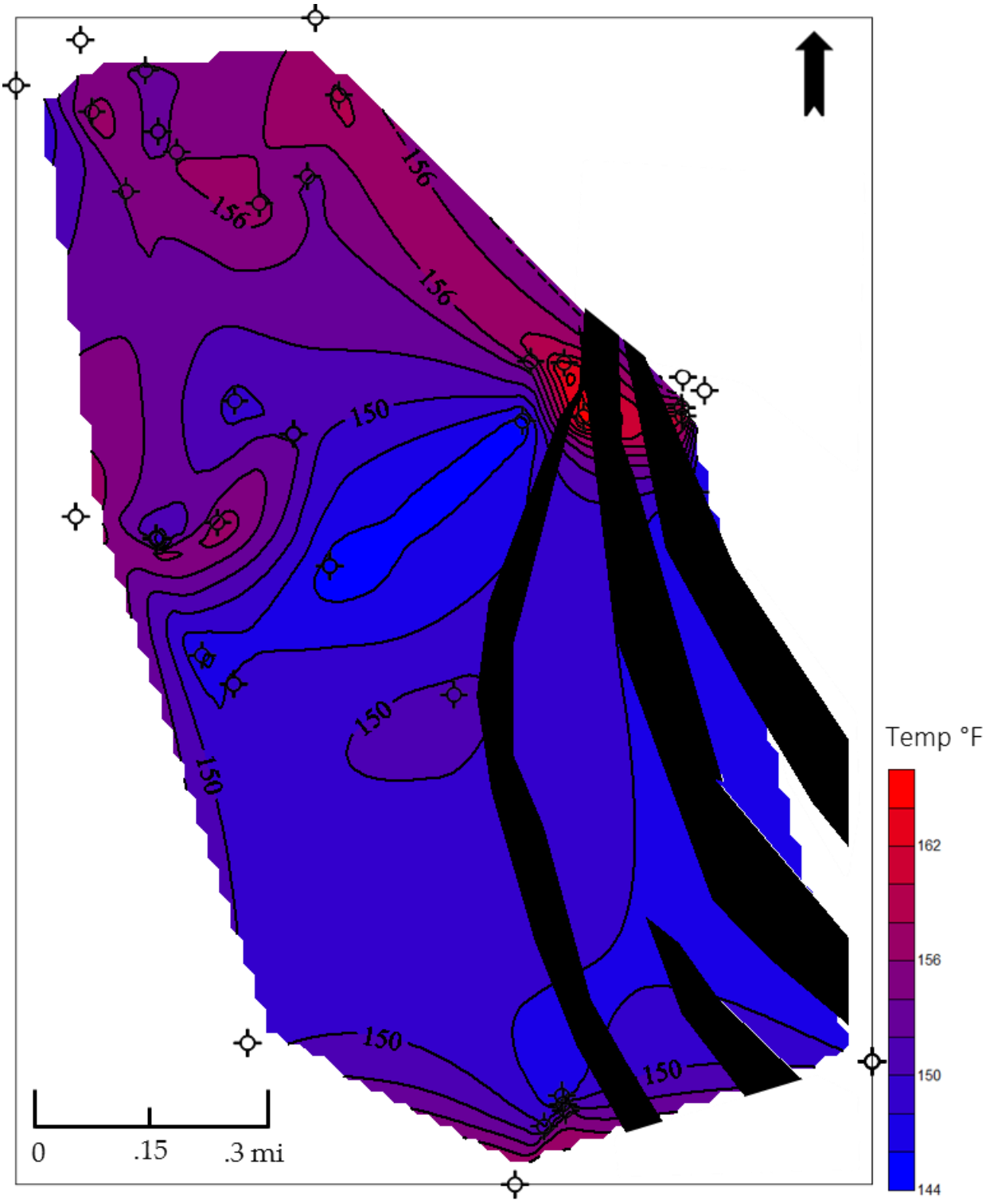

Figure 24: Fault polygons in black superimposed on temperature map at 6000 ft (2000 m) SSTVD. Notice large temperature anomaly in northeast corner of map aligns with convergence of three faults

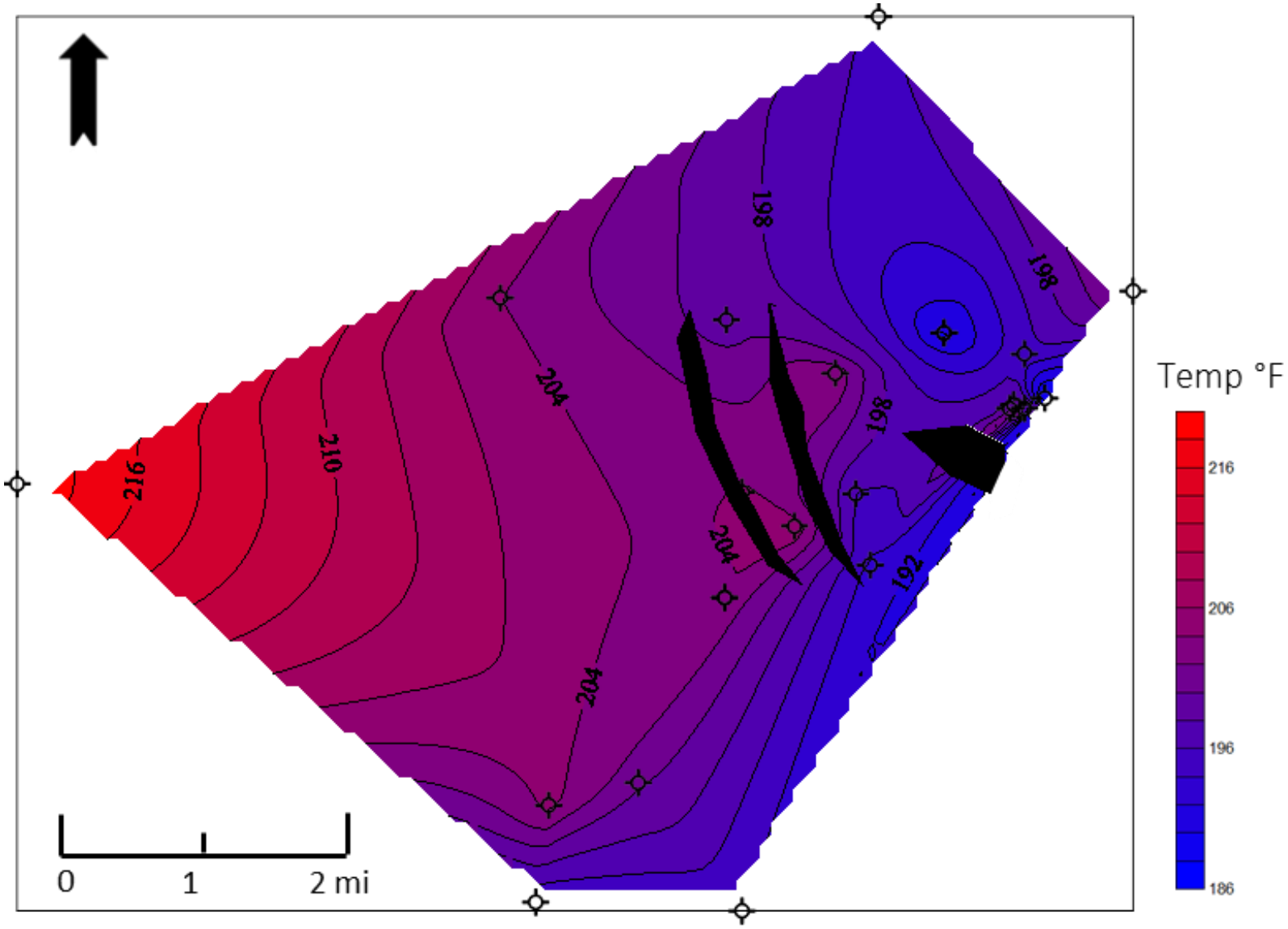

Figure 25: Fault polygons in black superimposed on temperature map at 10,000 ft (3000 m) SSTVD. Notice two temperature anomaly in central portion of map aligns with fault polygon locations

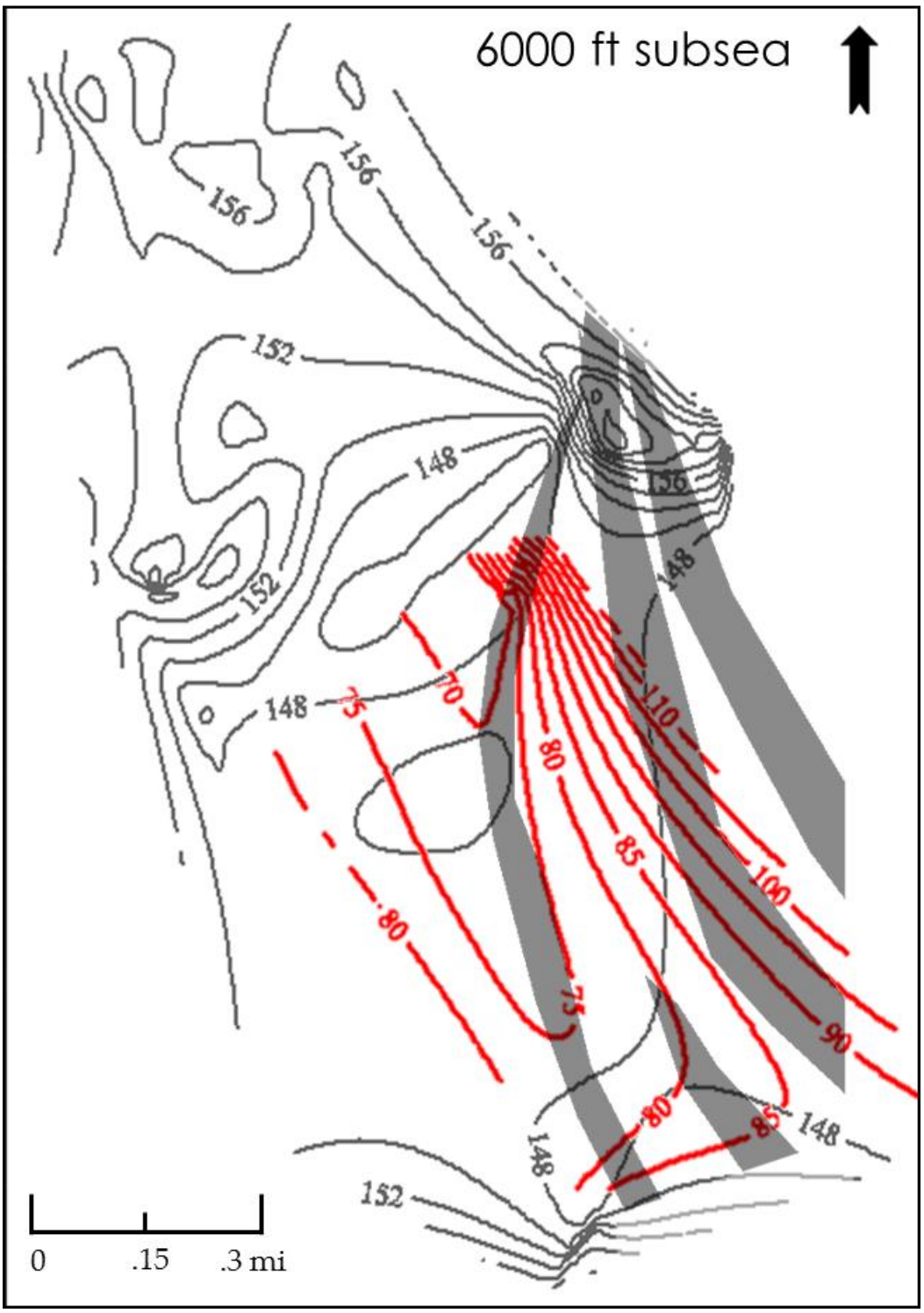

Figure 26: Salinity map and fault polygons superimposed on temperature map at 6000 ft (2000 m) SSTVD. Temperature contours in dark grey, salinity contours in red, and fault polygons in transparent grey. Notice that salinity increases towards area where the fault polygons converge

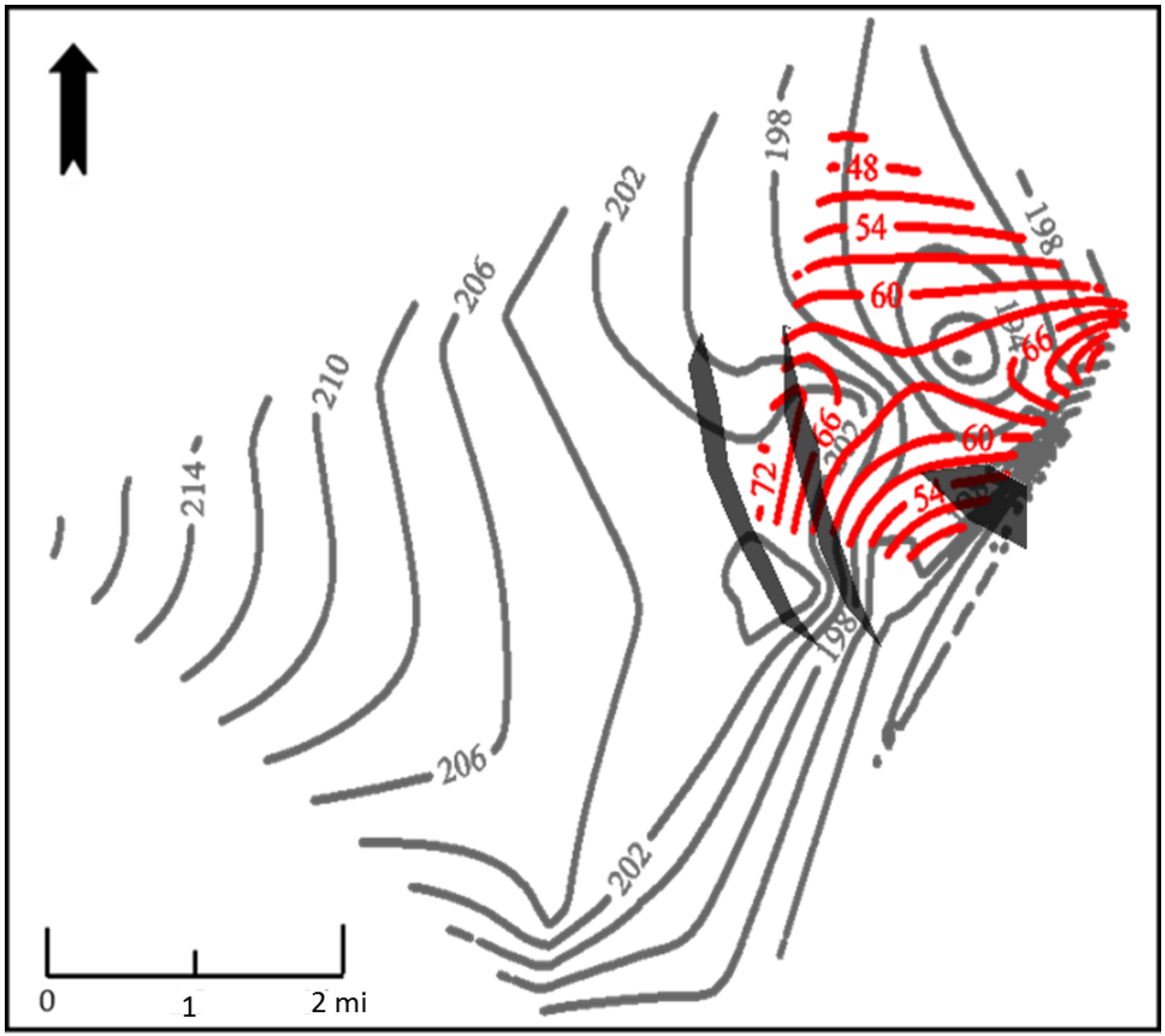

Figure 27: Salinity map and fault polygons superimposed on temperature map at 10,000 ft (3000 m) SSTVD. Temperature contours in dark grey, salinity contours in red, and fault polygons in transparent grey. Notice that salinity increases towards temperature anomalies and fault polygons

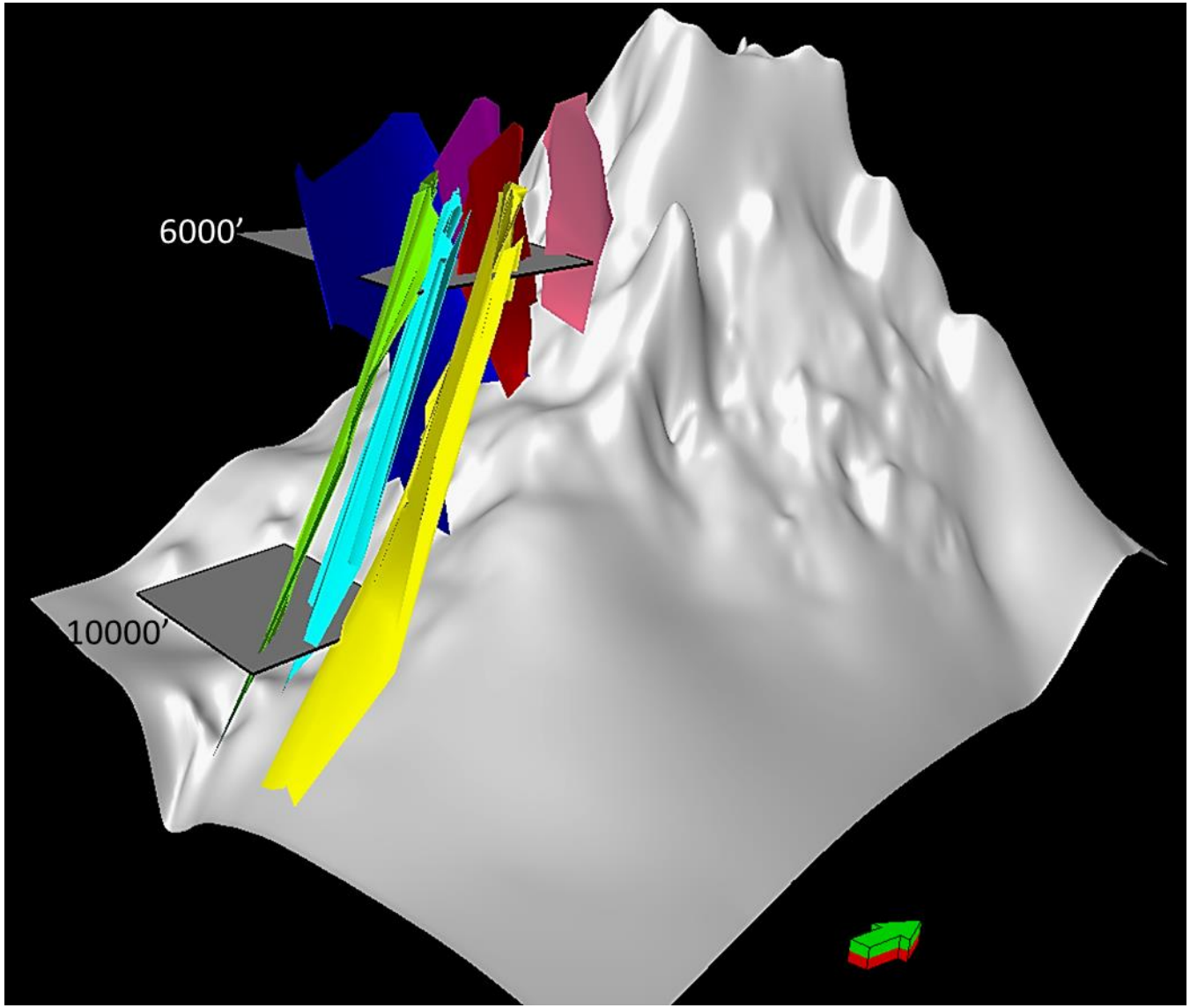

Figure 28: 3D image with 3X vertical exaggeration of interpreted fault planes and top of salt from seismic. Top of salt in white, faults planes in various colors, horizontal grey rectangles are temperature map locations, green arrow indicates north

Conclusions

As Bruno and Hanor (2003), Steen et al. (2011), and Richards (2013) all hypothesized, lithology controls the distribution of hypersaline formation waters in the vicinity of salt structures, with hypersaline fluids preferentially occupying sand-dominated sections, rather than shale-dominated sections. The middle and deepest hydrogeologic regimes as seen in other studies throughout offshore Gulf of Mexico were identified in this study area. The temperature and salinity distribution here is consistent with ormation waters migrating vertically upwards through faults from depth, and in some cases the faults are close enough to the salt to allow dissolution of the salt and the formation and migration of hypersaline brines away from the salt structure. Formation waters at all depths in this study area were at near-marine salinity levels before faulting commenced. Fault activity continued after hypersaline formation waters migrated away from the salt structure, and thus, formation waters have been horizontally compartmentalized by the faults, as seen in the Bruno and Hanor (2003) and Steen et al. (2011) studies. Better data coverage for the salinity and temperature maps, especially in the vicinity of the highly faulted regions, would help to clarify the conclusion that temperature and salinity increase in the vicinity of faulting. Also, more temperature and salinity maps could be created at several more depths in order to achieve a better three-dimensional model of how temperature and salinity is changing throughout the entire faulted depth interval. In order to interpret the best representation of the actual geometry of the faults, it would also be of interest to obtain a more accurate seismic velocity model derived from check-shot data, rather than a simple constant velocity estimation from sonic logs.

References

Bennett, S. S., and Hanor, J. S., 1987. Dynamics of subsurface salt dissolution at the Welsh Dome, Louisiana Gulf Coast: Dynamical Geology of Salt and Related Structures, p. 653-677.

Bense, V.F., and Person, M.A., 2006. Faults as conduit-barrier systems to fluid flow in siliciclastic sedimentary aquifers: Water Resources Research, p.42.

Blackwell, D.D., and Richards, M.C., 2004. Geothermal Map of North America: AAPG, 1 sheet, scale 1:6,500,000

Bruno, R.S., and Hanor, J.S., 2003. Large-scale fluid migration driven by salt dissolution, Bay Marchand dome, offshore Louisiana: Gulf Coast Association of Geological Societies Transactions, v. 53, p. 97-107.

Daugherty, W. J., 2012. Spatial variation analysis of salinity to determine fluid flow pathways and reservoir compartmentalization in a deepwater Gulf of Mexico field. M.S. Thesis, Louisiana State University, Department of Geology and Geophysics.

Evans, D. G., and Nunn, J. A., 1989. Free thermohaline convection in sediments surrounding a salt column: Journal of Geophysical Research: Solid Earth (1978–2012), v. 94, no. B9, p. 12413-12422.

Evans, D.G., Nunn, J.A., and Hanor, J.S., 1991. Mechanisms driving groundwater flow near salt domes: Geophysical Research Letters, v. 18, p. 927-930.

Frey, M.G., and Grimes, W.H., 1970. Bay Marchand-Timbalier Bay-Caillou Island Salt Complex, Louisiana: Bulletin American Association of Petroleum Geologists Memoir, n. 14, p. 277-291.

Galloway, W.E., 2009. Gulf of Mexico: GEOExPro, v. 6, n. 3.

Galloway, W.E., Bebout, D.G., Fisher W.L., Cabrera-Castro R., Lugo-Rivera J.E., Scott T.M., 1991. Cenozoic. In: The Geology of North America: the Gulf of Mexico Basin p. 245–324.

Galloway, W.E., Ganey-Curry, P.E., Li, X., and Buffler, R.T., 2000. Cenozoic depositional history of the Gulf of Mexico basin: AAPG Bulletin, v. 89, n. 11, p. 1743-1774.

Hanor, J.S., and Mercer, J. A., 2010. Spatial variations in the salinity of pore waters in northern deep water Gulf of Mexico sediments: implications for pathways and mechanisms of solute transport: Geofluids, v. 10, no. 1-2, p. 83-93.

Hanor, J.S., and Sassen, R., 1990, Evidence for large scale vertical and lateral migration of formation waters, dissolved salt, and crude oil in the Louisiana Gulf Coast: In D. Schumacher and B.F. Perkins (eds.), Proc. 9th Annual Res. Conf., Gulf Coast Section, Society of Economic Paleontologists and Mineralogists Foundation, p. 283-296.

Jolly, S. J., Fisher, Q.J., and Ainsworth, R.B., 2010. Reservoir compartmentalization: an introduction: Geological Society, London, Special Publications, v. 347, p. 1-8.

Kehle, R.O., 1971. Geothermal survey of North America, 1971 Annual Progress Report: Tulsa, American Association of Petroleum Geologists, p. 31.

Lewis, C. R., and Rose, S. C., 1970. A theory relating high temperatures and overpressures: Journal of Petroleum Technology, v. *22*, p. 11-16.

Li, Y., Nowlin, W.D., and Reid, R.O., 1997. Mean hydrographic fields and their interannual variability over the Texas-Louisiana continental shelf in spring, summer and fall: Journal of Geophysical Research, v. 102, p. 1027-1049.

Lin, G., and Nunn, J.A., 1997. Evidence for recent migration of geopressured fluids along faults in Eugene Island, Block 330, offshore Louisiana, from estimates of pore water salinity: Transactions Gulf Coast Association of Geological Societies, v. 47, p. 419-424.

Ranganathan, V., and Hanor, J. S., 1989. Perched brine plumes above salt domes and dewatering of geopressured sediments: Journal of Hydrology, v. 110, no. 1, 63-86.

Revil, A., Cathles, L. M., Losh, S., and Nunn, J. A., 1998. Electrical conductivity in shaly sands with geophysical applications: Journal of Geophysical Research, v. 103, no. B10, p. 23925-3936.

Richards, L., 2013. Spatial variations in salinity and temperature around the Bay Marchand salt dome, offshore Louisiana. M.S. Thesis, Louisiana State University, Department of Geology and Geophysics.

Salvador, A., 1991. Origin and development of the Gulf of Mexico basin: The Gulf of Mexico Basin, p. 389-444.

Steen, A. K., Nunn, J.A., and Hanor, J.S., 2011. Indications of formation water flow and compartmentalization on the flank of a salt structure derived from salinity and seismic data: Geofluids, v. 11, no. 2, p. 199-208.

Waxman, M.H., and Smits, L.J.M., 1968. Electrical conductivities in oil-bearing shaly sands: Society of Petroleum Engineers Journal, v. 8, no. 2.

Appendix I: Porosity calibration

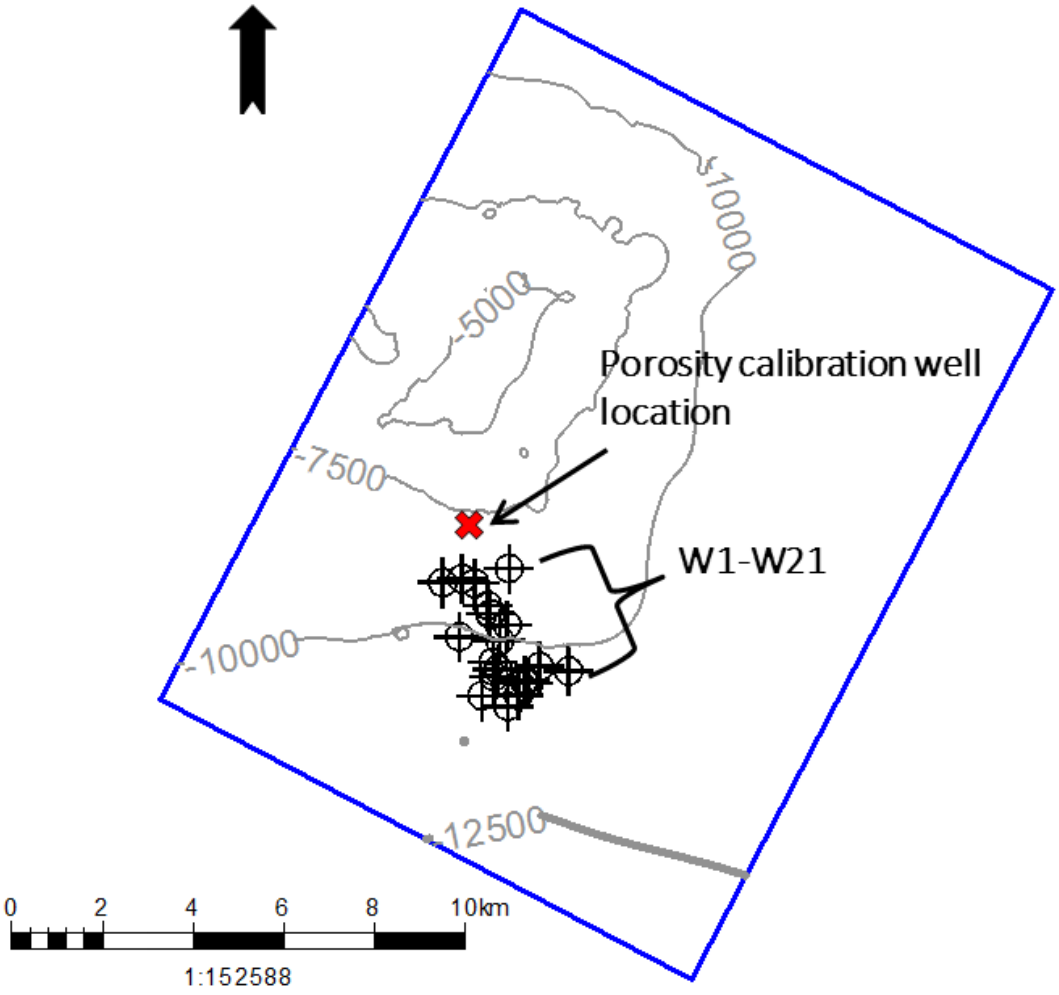

Figure 28: Location map for well used in porosity calibration for the Revil et al. (1998) method. Location of calibration well indicated by red X

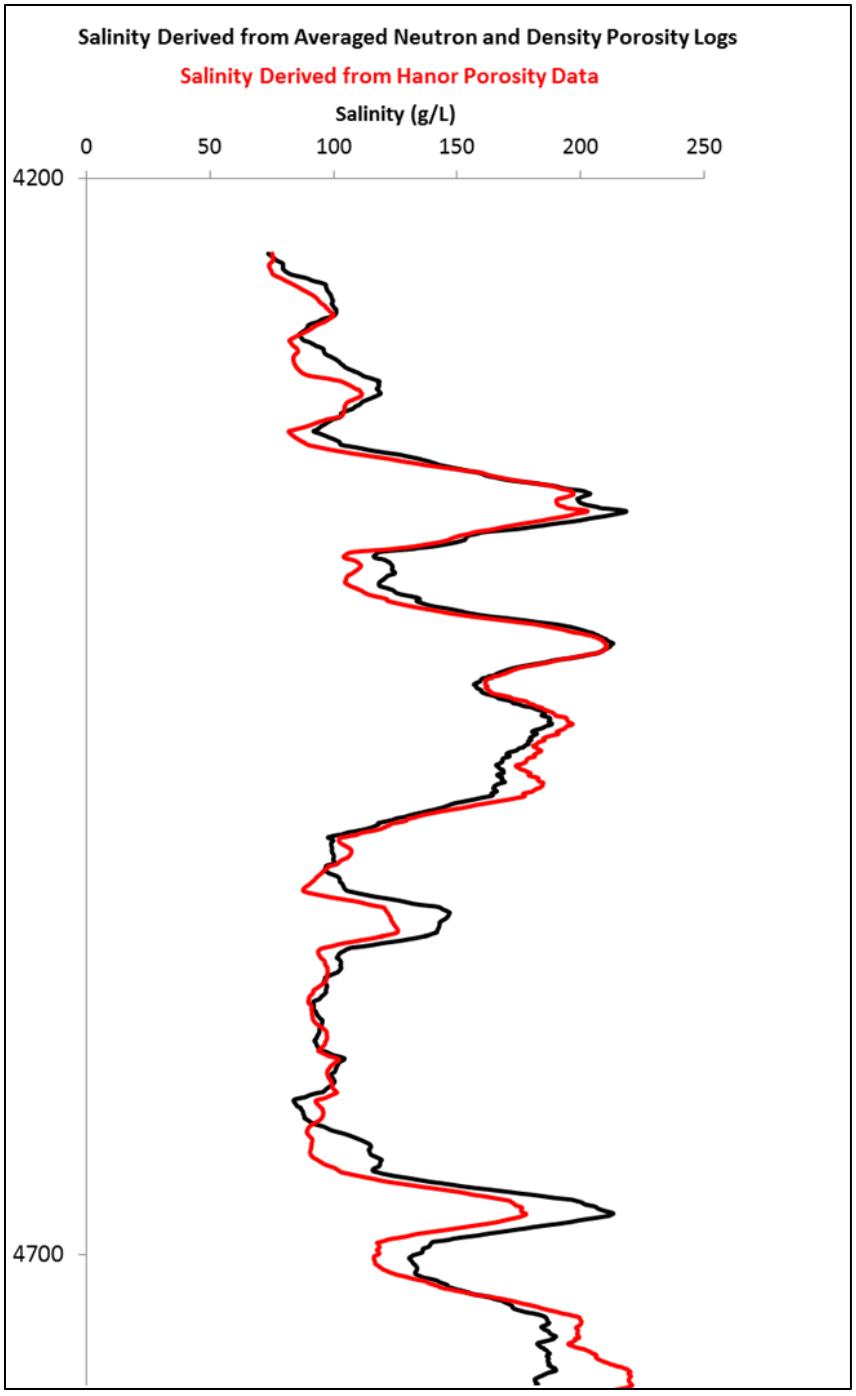

Figure 29a: Two salinity curves derived from porosity values from averaged neutron and density porosity curves (black) and Hanor (personal communication 2014) porosity data

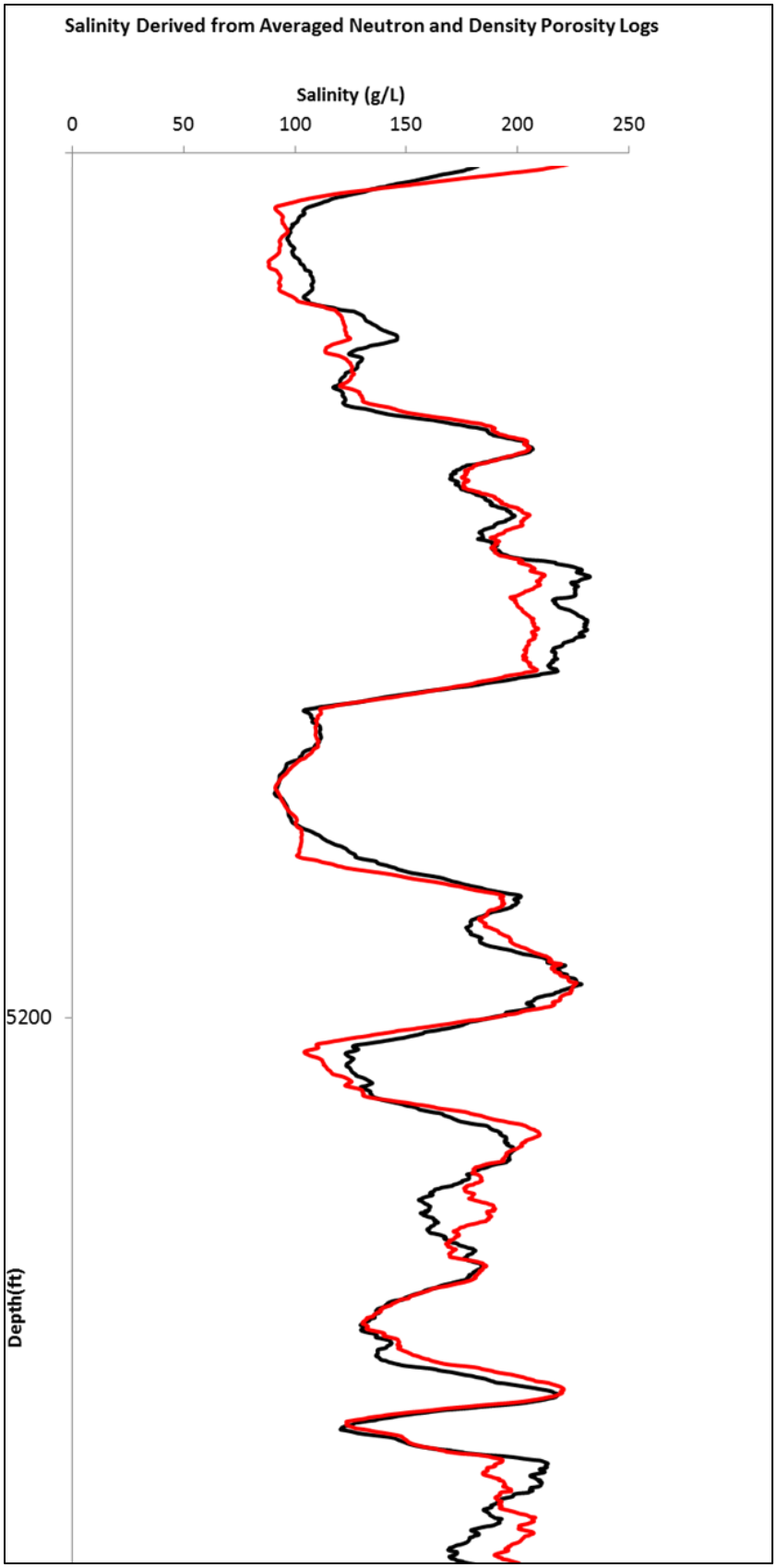

Figure 29b: Figure Continued

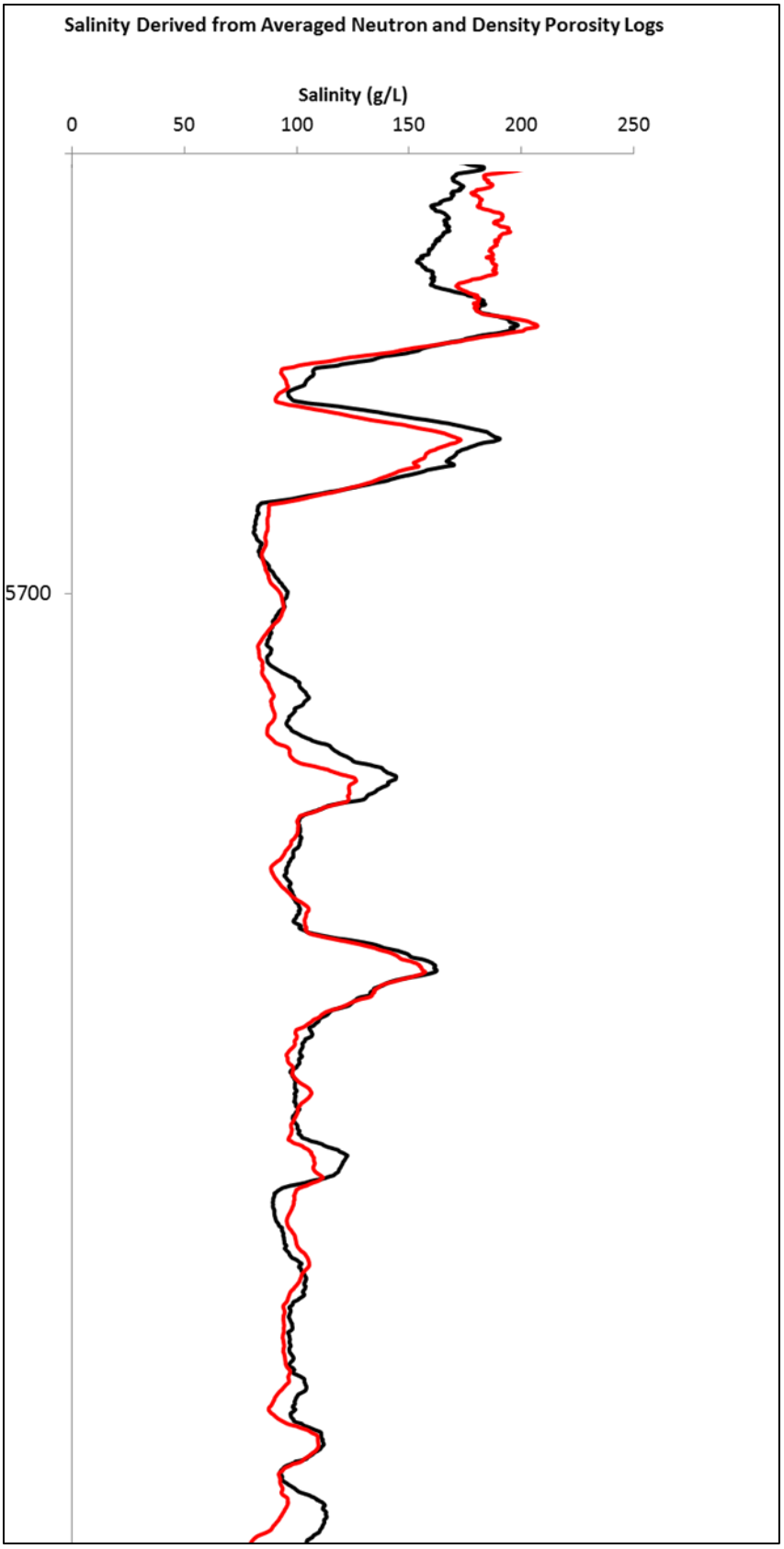

Figure 29c: Figure Continued

Appendix II: W2 Salinity curve with and without moving average

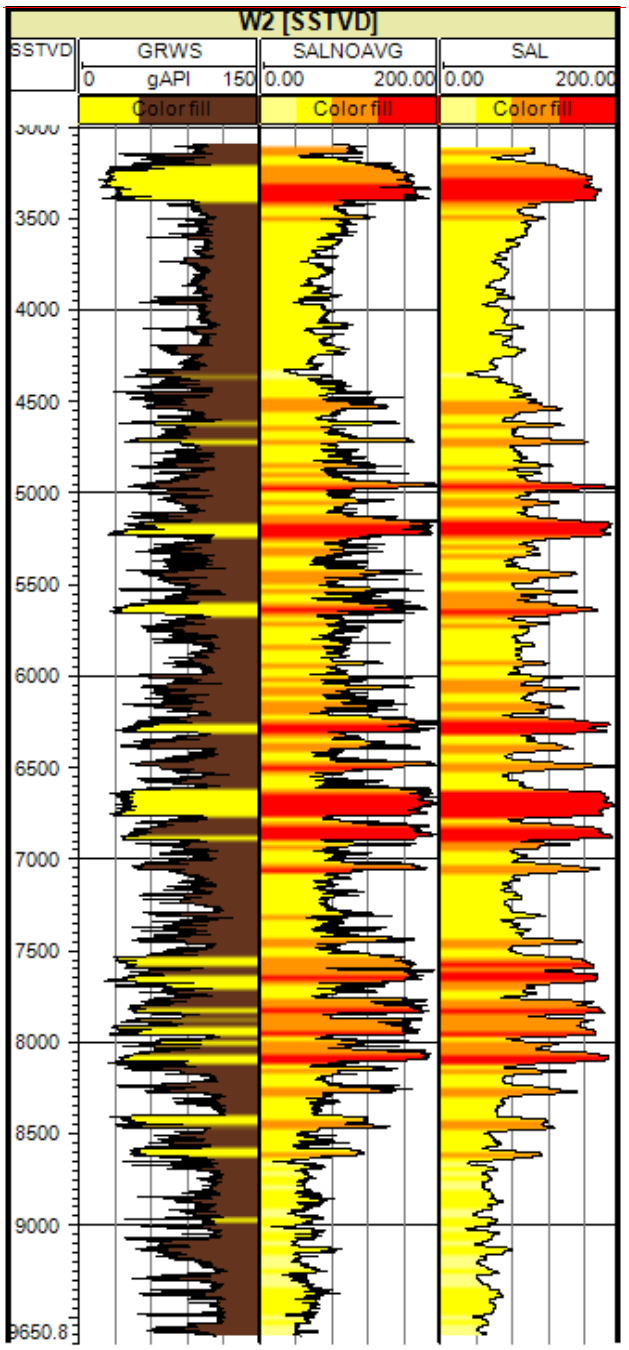

Figure 30: Well W2 gamma ray curve on far left, salinity curve without moving average in middle, and salinity curve with moving average on far right

Appendix III: Gamma and salinity curves for all wells in salinity well set

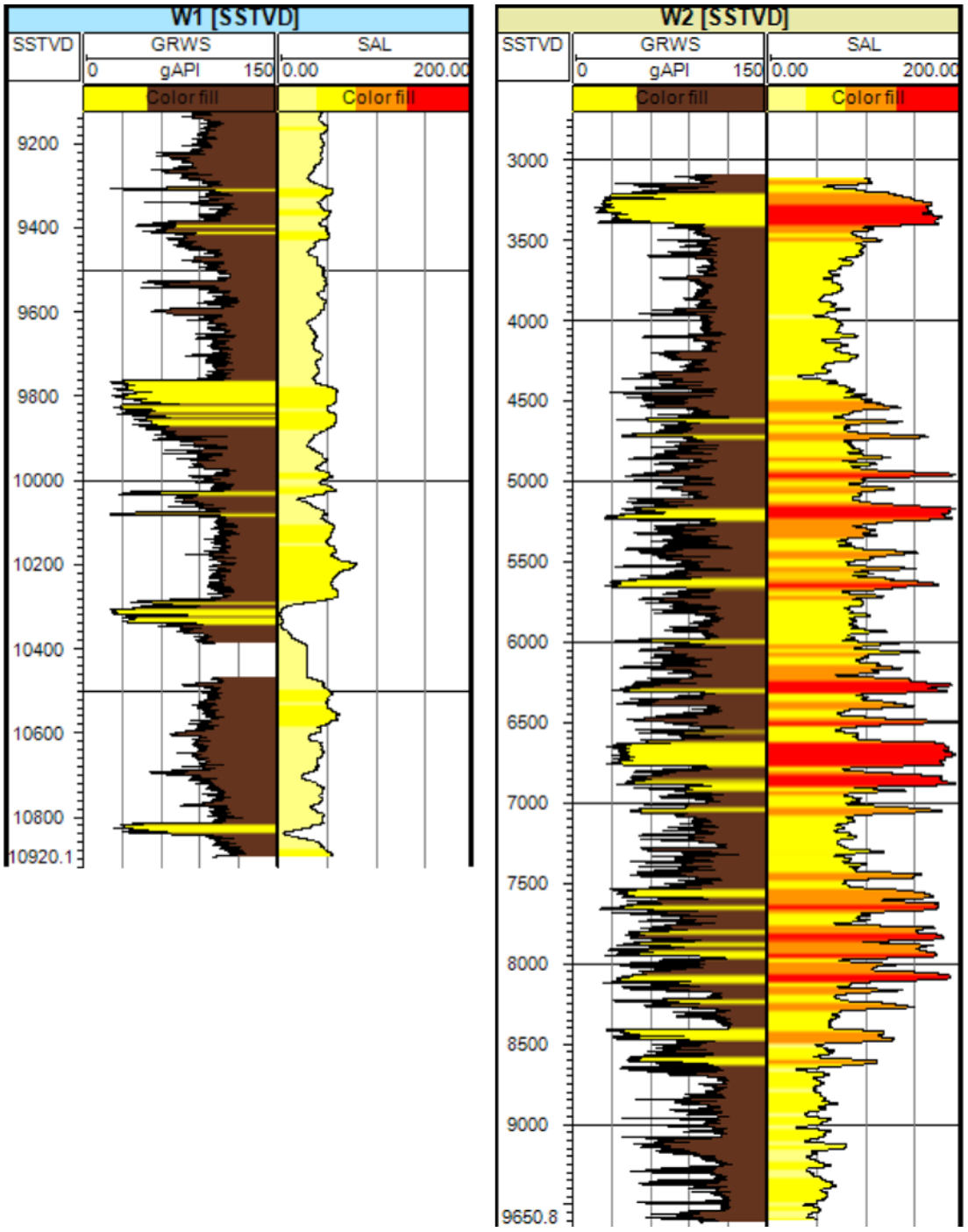

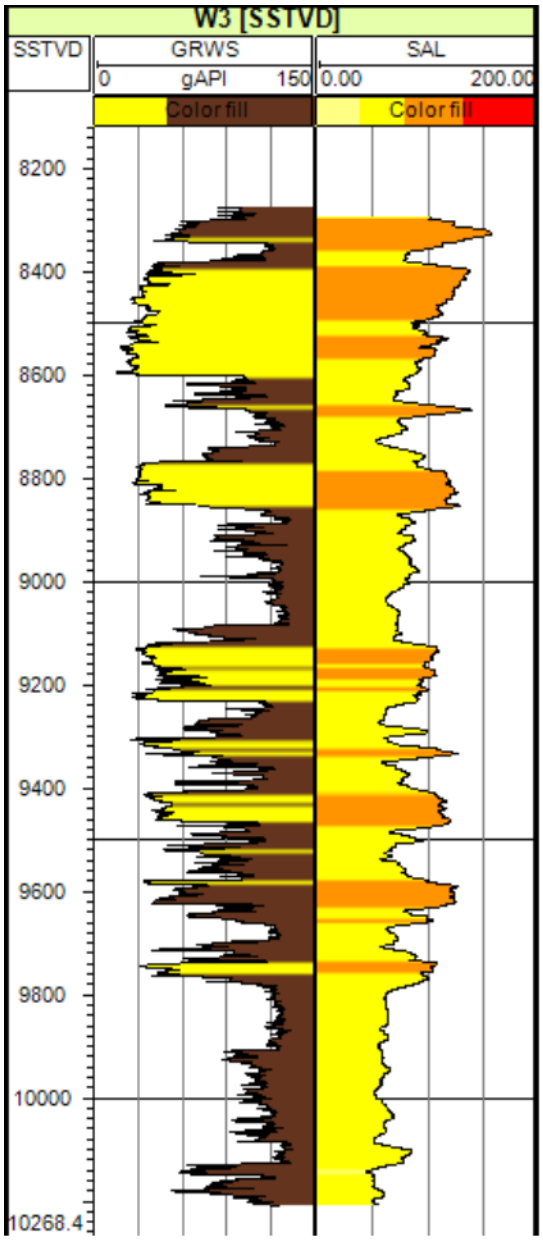
W3 [SSTVD]
SSTVD
GRWS
0 gAPI 150
SAL
0.00 200.00
Color fill
Color fill
8200
8400
8600
8800
9000
9200
9400
9600
9800
10000
10268.4

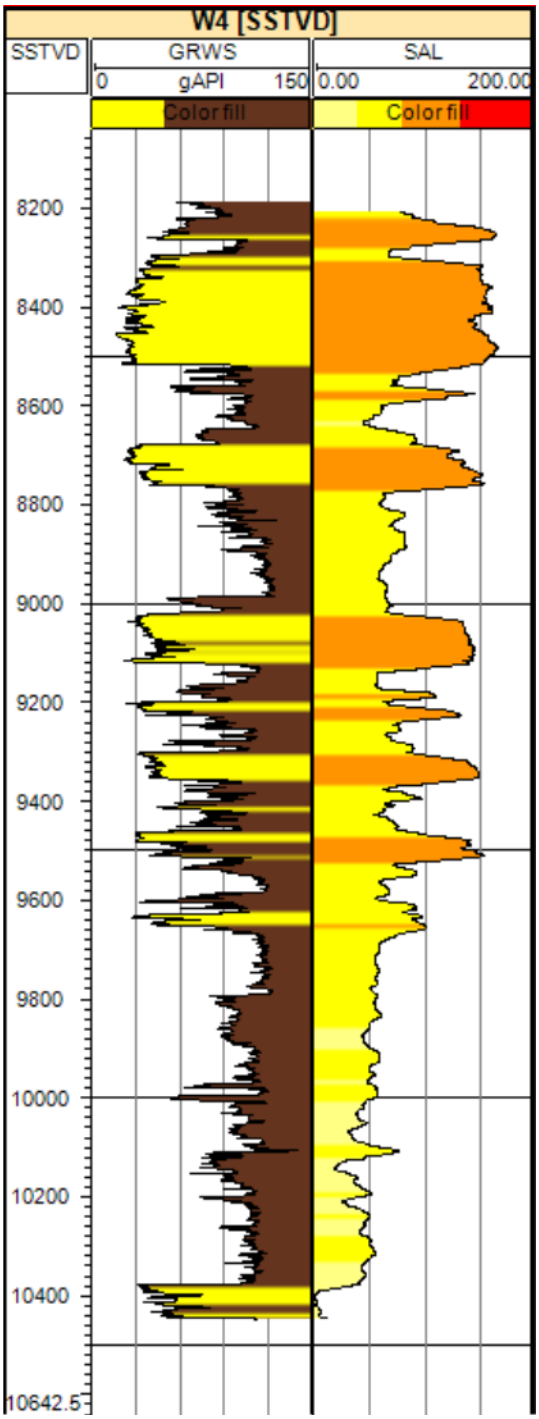
W4 [SSTVD]
SSTVD
GRWS
0 gAPI 150
SAL
0.00 200.00
Color fill
Color fill
8200
8400
8600
8800
9000
9200
9400
9600
9800
10000
10200
10400
10642.5

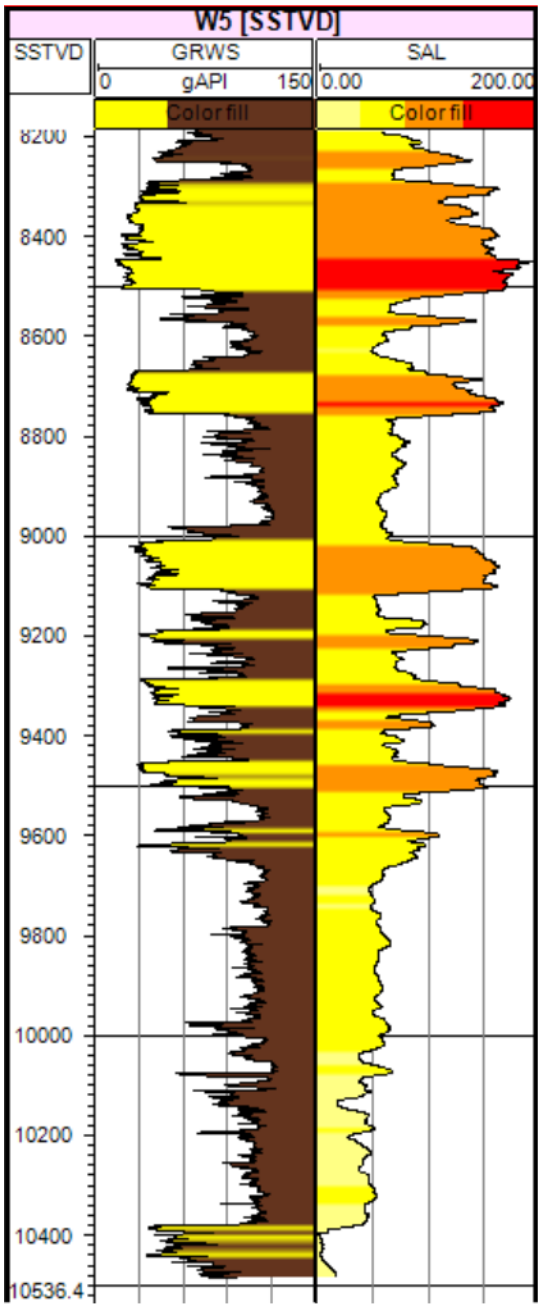
W5 [SSTVD]
SSTVD
GRWS
0 gAPI 150
SAL
0.00 200.00
Color fill
Color fill
8200
8400
8600
8800
9000
9200
9400
9600
9800
10000
10200
10400
10536.4

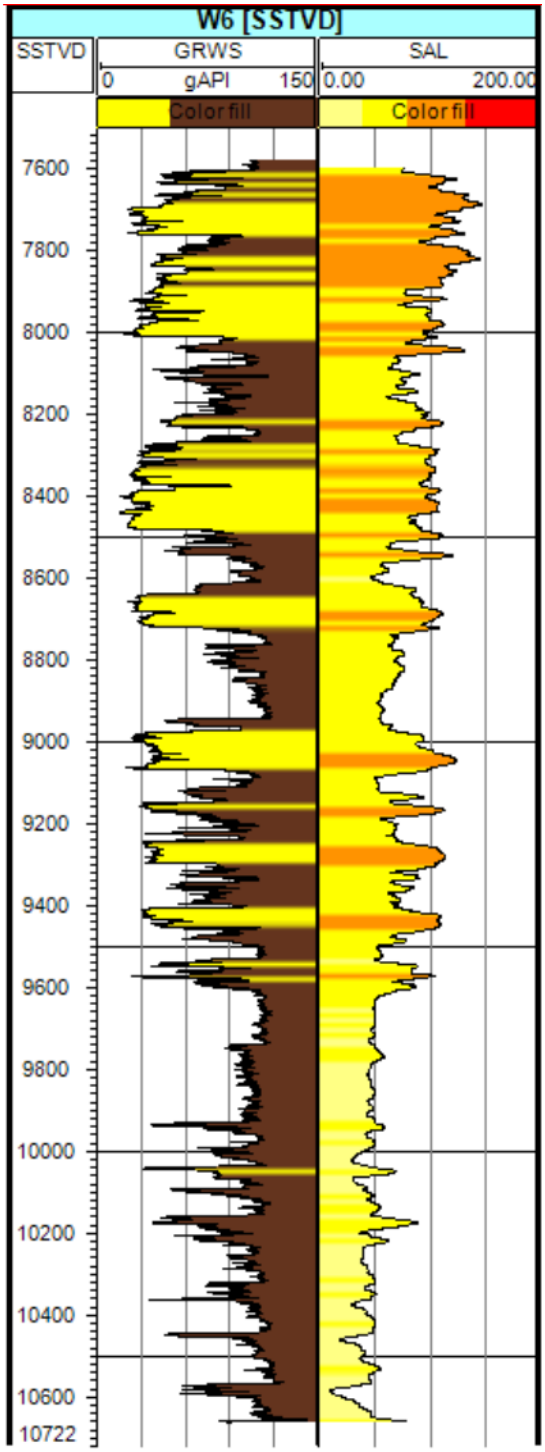
W6 [SSTVD]
SSTVD
GRWS
0 gAPI 150
SAL
0.00 200.00
Color fill
Color fill
7600
7800
8000
8200
8400
8600
8800
9000
9200
9400
9600
9800
10000
10200
10400
10600
10722

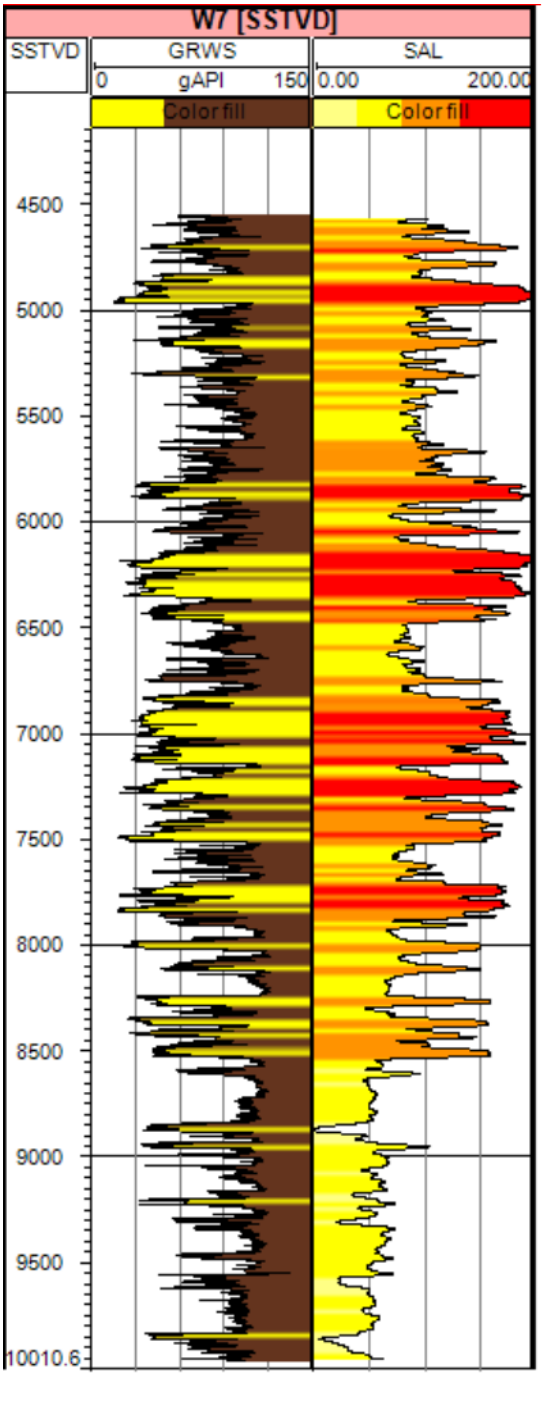
W7 [SSTVD]
SSTVD
GRWS
0 gAPI 150
SAL
0.00 200.00
Color fill
Color fill
4500
5000
5500
6000
6500
7000
7500
8000
8500
9000
9500
10010.6

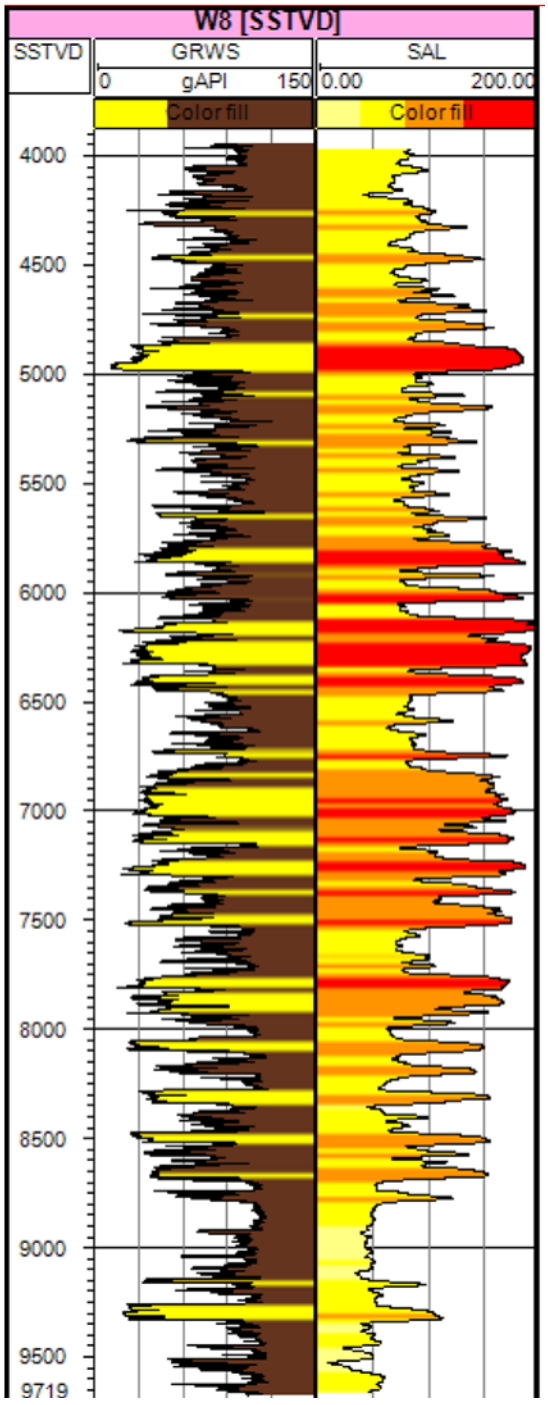
W8 [SSTVD]
SSTVD
GRWS
0 gAPI 150
SAL
0.00 200.00
Color fill
Color fill
4000
4500
5000
5500
6000
6500
7000
7500
8000
8500
9000
9500
9719

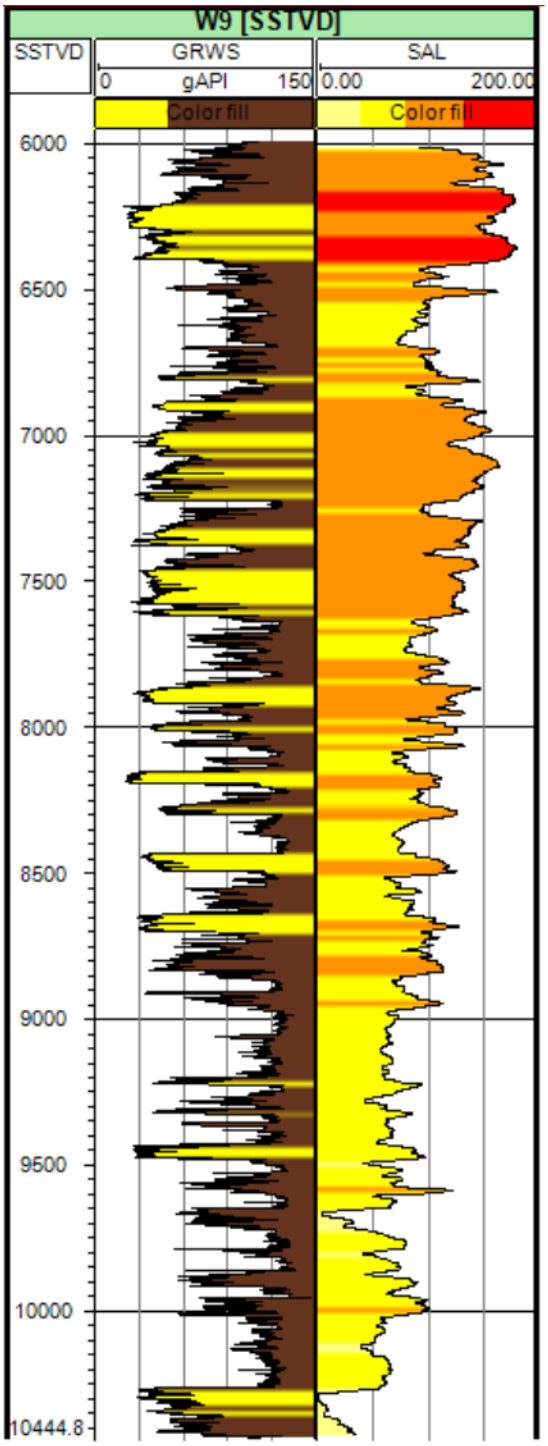
W9 [SSTVD]
SSTVD
GRWS
0 gAPI 150
SAL
0.00 200.00
Color fill
Color fill
6000
6500
7000
7500
8000
8500
9000
9500
10000
10444.8

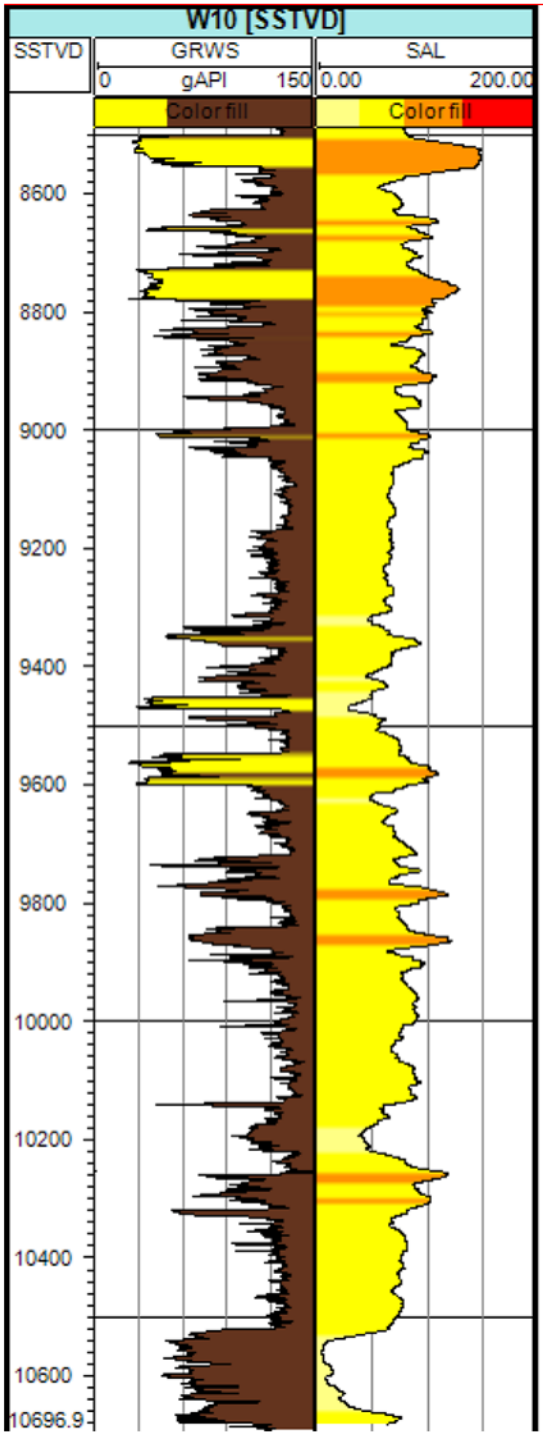
W10 [SSTVD]
SSTVD
GRWS
0 gAPI 150
SAL
0.00 200.00
Color fill
Color fill
8600
8800
9000
9200
9400
9600
9800
10000
10200
10400
10600
10696.9

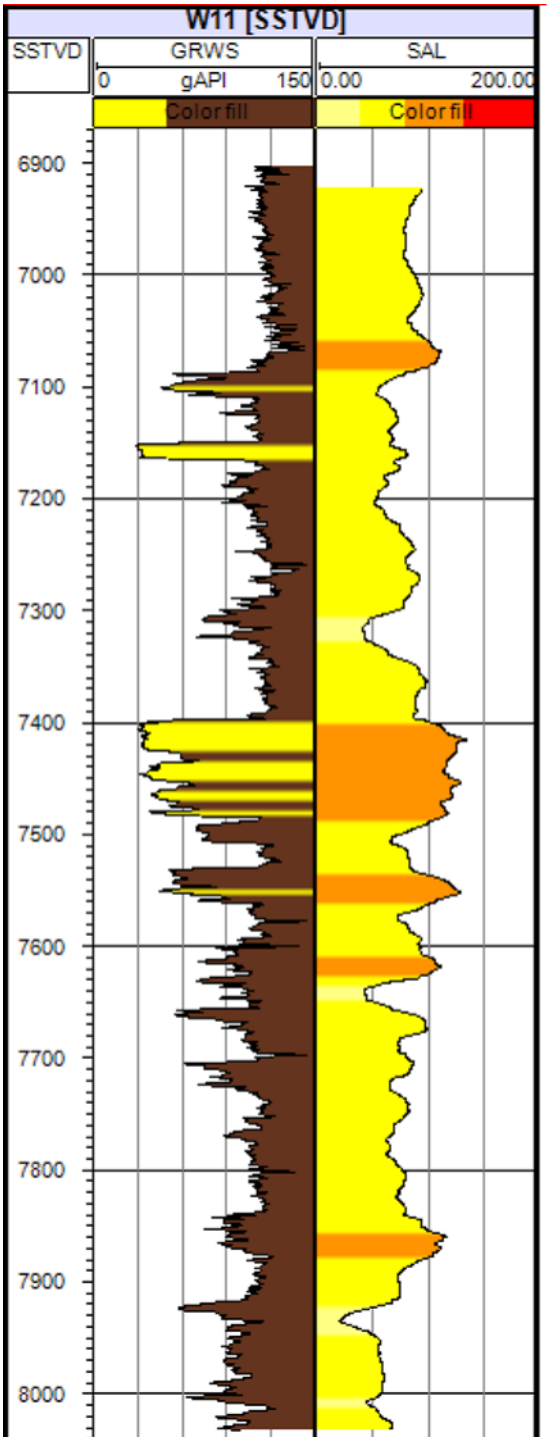
W11 [SSTVD]
SSTVD
GRWS
0
gAPI
150
SAL
0.00
200.00
Color fill
Color fill
6900
7000
7100
7200
7300
7400
7500
7600
7700
7800
7900
8000

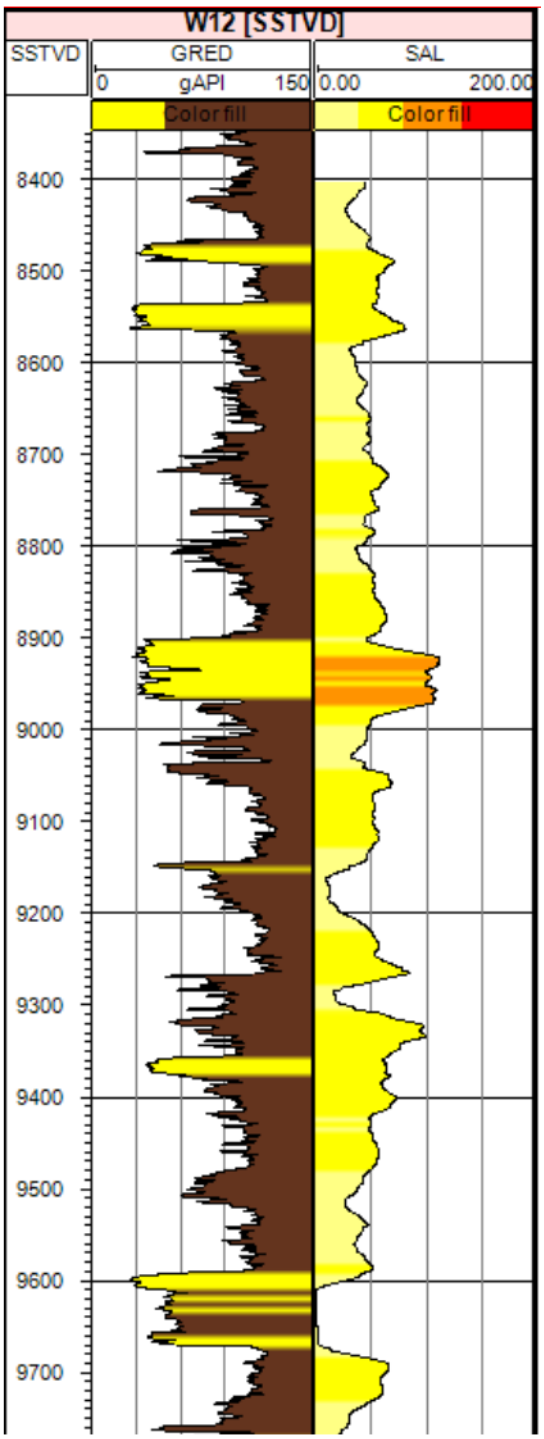
W12 [SSTVD]
SSTVD
GRED
0
gAPI
150
SAL
0.00
200.00
Color fill
Color fill
8400
8500
8600
8700
8800
8900
9000
9100
9200
9300
9400
9500
9600
9700

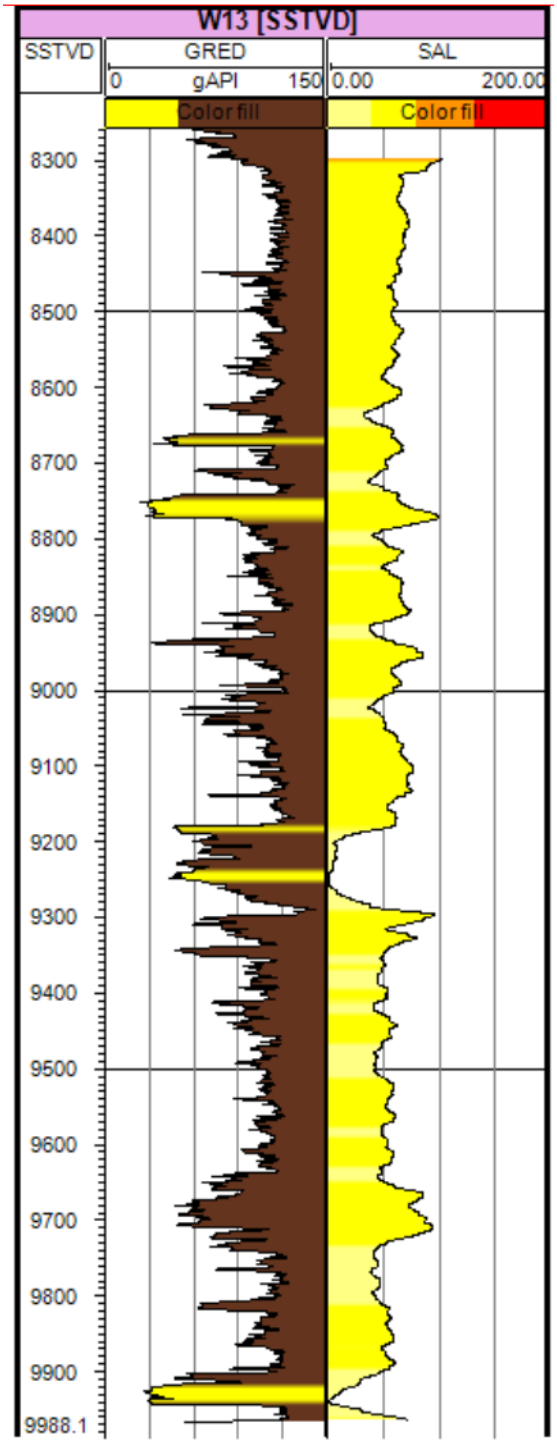
W13 [SSTVD]
SSTVD
GRED
0
gAPI
150
SAL
0.00
200.00
Color fill
Color fill
8300
8400
8500
8600
8700
8800
8900
9000
9100
9200
9300
9400
9500
9600
9700
9800
9900
9988.1

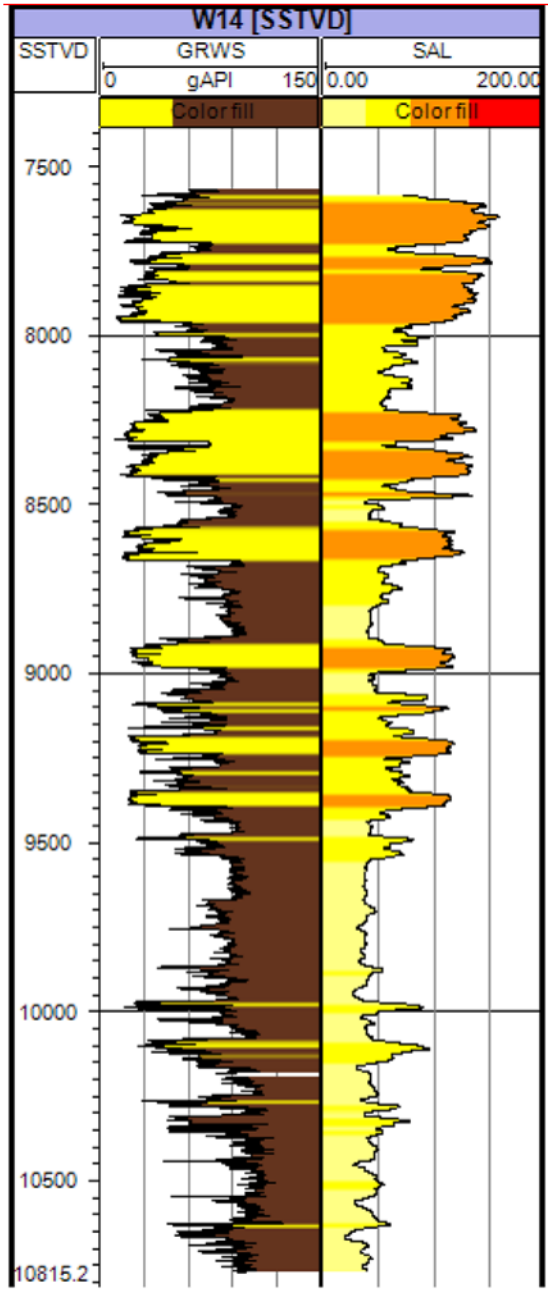
W14 [SSTVD]
SSTVD
GRWS
0
gAPI
150
SAL
0.00
200.00
Color fill
Color fill
7500
8000
8500
9000
9500
10000
10500
10815.2

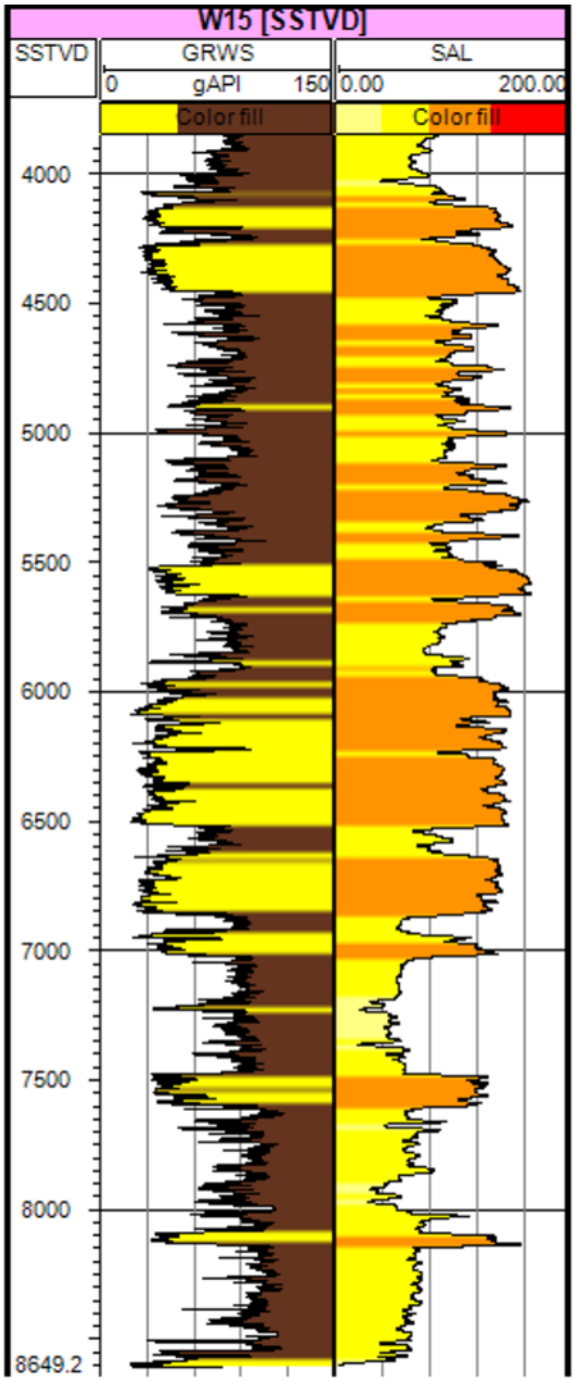
W15 [SSTVD]
SSTVD
GRWS
0 gAPI 150
SAL
0.00 200.00
Color fill
Color fill
4000
4500
5000
5500
6000
6500
7000
7500
8000
8649.2

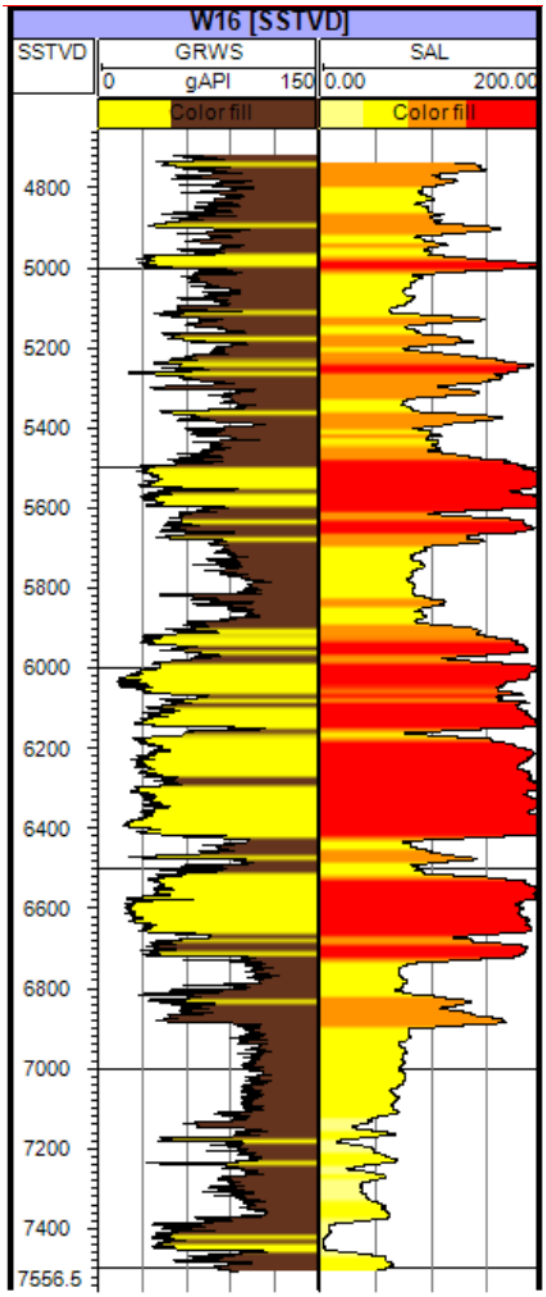
W16 [SSTVD]
SSTVD
GRWS
0 gAPI 150
SAL
0.00 200.00
Color fill
Color fill
4800
5000
5200
5400
5600
5800
6000
6200
6400
6600
6800
7000
7200
7400
7556.5

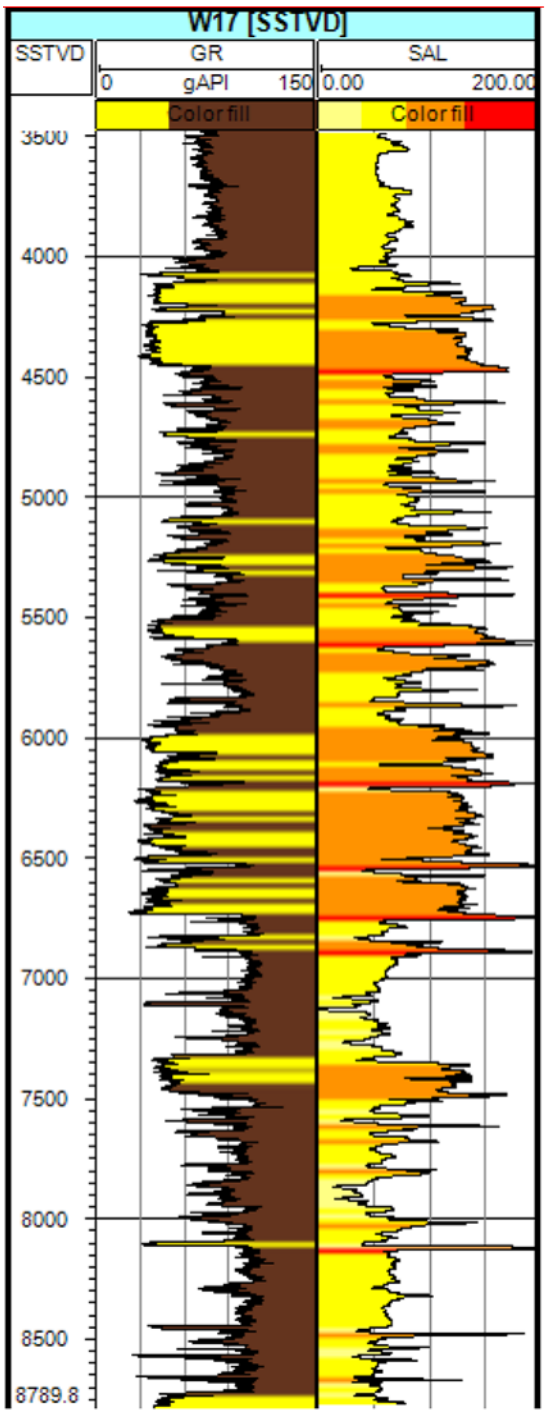
W17 [SSTVD]
SSTVD
GR
0 gAPI 150
SAL
0.00 200.00
Color fill
Color fill
3500
4000
4500
5000
5500
6000
6500
7000
7500
8000
8500
8789.8

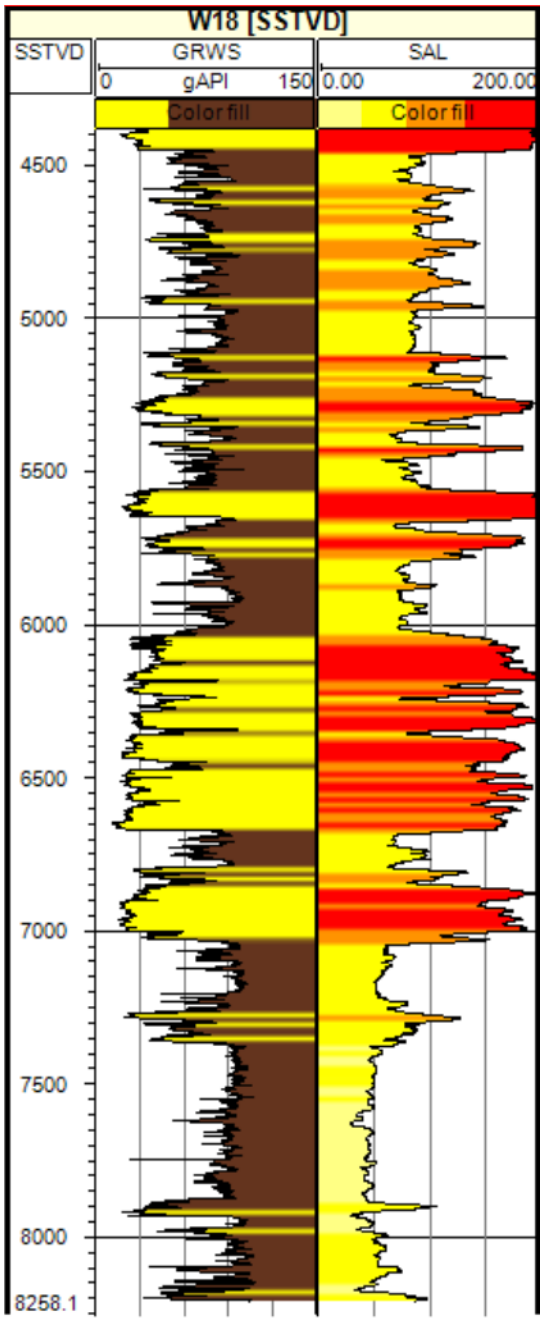
W18 [SSTVD]
SSTVD
GRWS
0 gAPI 150
SAL
0.00 200.00
Color fill
Color fill
4500
5000
5500
6000
6500
7000
7500
8000
8258.1

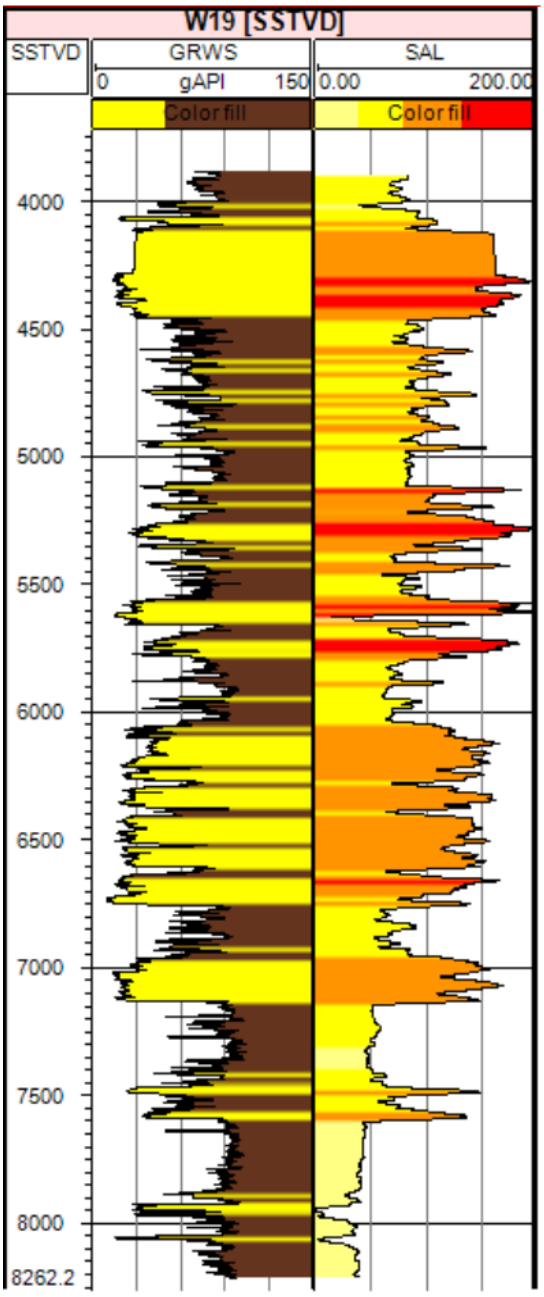
W19 [SSTVD]
SSTVD
GRWS
0 gAPI 150
SAL
0.00 200.00
Color fill
Color fill
4000
4500
5000
5500
6000
6500
7000
7500
8000
8262.2

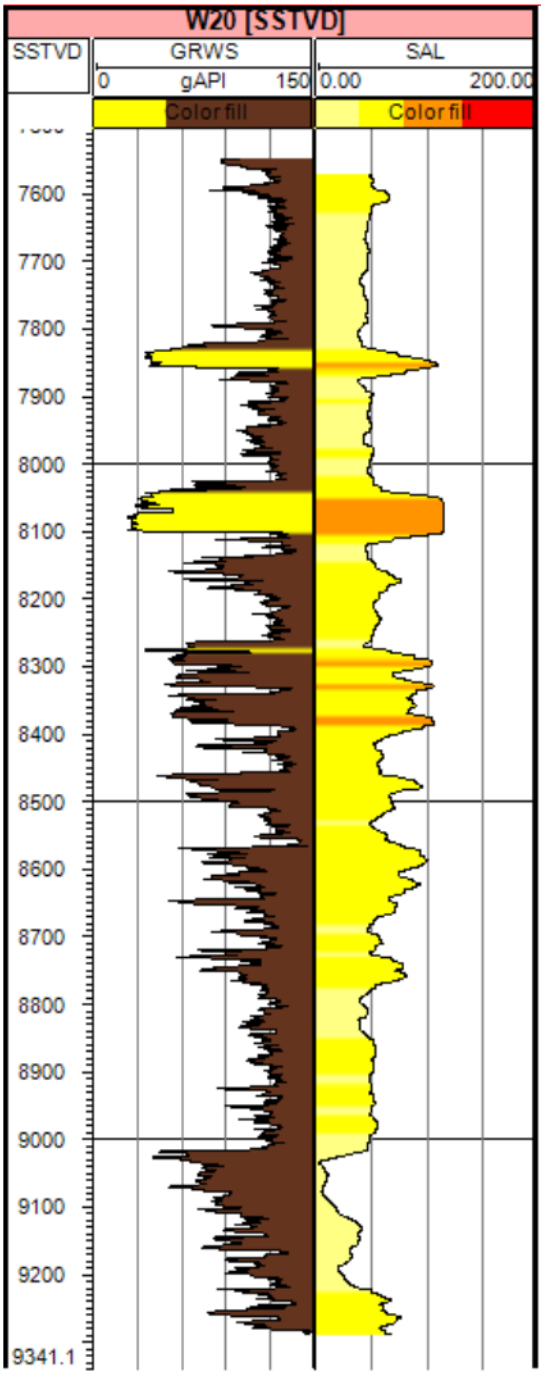
W20 [SSTVD]
SSTVD
GRWS
0 gAPI 150
SAL
0.00 200.00
Color fill
Color fill
7600
7700
7800
7900
8000
8100
8200
8300
8400
8500
8600
8700
8800
8900
9000
9100
9200
9341.1

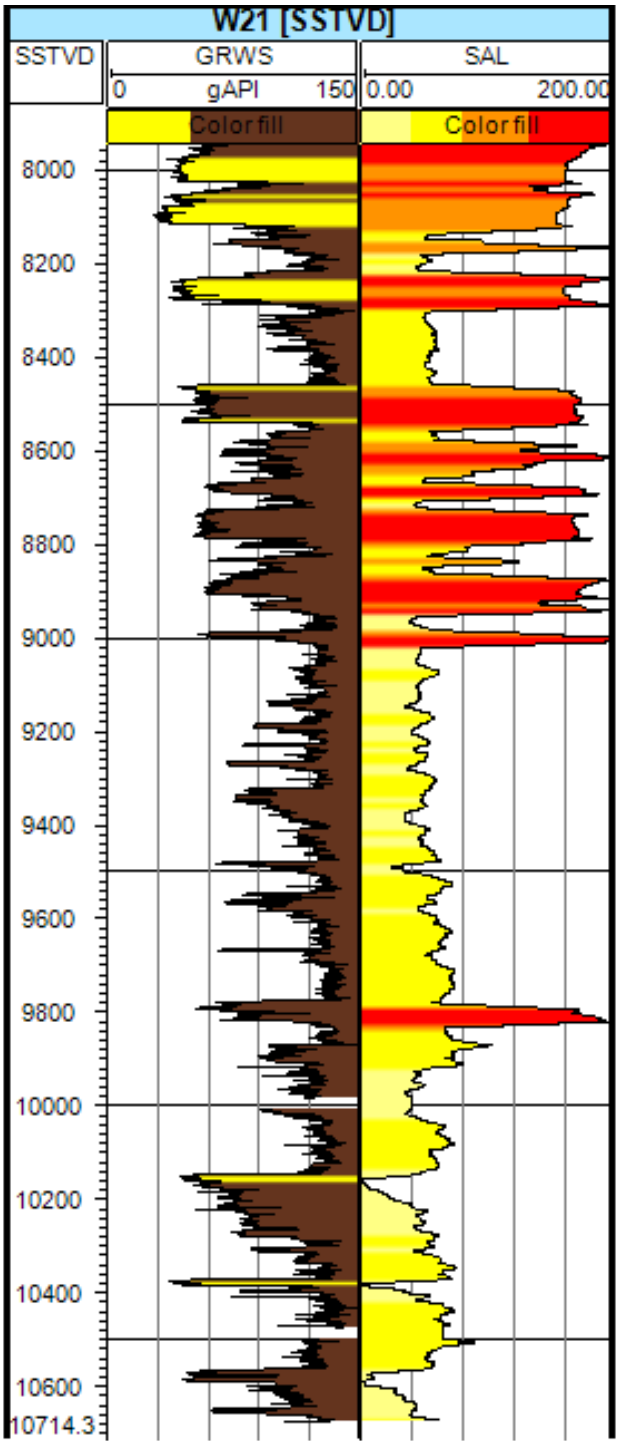
W21 [SSTVD]
SSTVD
GRWS
0
gAPI
150
Color fill
SAL
0.00
200.00
Color fill
8000
8200
8400
8600
8800
9000
9200
9400
9600
9800
10000
10200
10400
10600
10714.3

Vita

Candice Marie McCollum was born in 1989 to Janet Cropper and West McCollum in Stuttgart, Germany. Her father served in the U.S. Army for 23 years, which resulted in six cross-continental/international moves (Germany, Hawaii, Washington, North Carolina, Utah, Colorado, and Alaska) throughout Candice's childhood and adolescence. After a lifetime spent as an Army brat, Candice's family settled in Wasilla, Alaska in 2006 where she graduated from high school and attended the University of Alaska in nearby Anchorage. She received her B.S. in Geology in 2011 and following graduation, she worked in remote Alaska as a core-logger for a junior gold exploration company for five months. Although daily helicopter flights and living and working amongst the picturesque Alaskan wilderness was enjoyable at her new job, she decided after roughing-it in the wilderness without flushing toilets and 12-hour work days that she'd rather work in a climate-controlled office with modern plumbing. Thereafter, she made the long drive from Alaska to Baton Rouge (five days and 4,289 mi) in 2012 with her then-fiancé to pursue her M.S. at Louisiana State University. In October 2012 she married Lanse Pettijohn at Magnolia Mansion in New Orleans. She is expected to receive her M.S. in Geology in August 2014 and will move to Midland, Texas in July 2014 with her husband, cat, two dogs, and two snakes to work for Concho Resources as a geologist.